References

Cravens, T. E. Physics of solar system plasmas, New York: Cambridge University Press, 1997.

Choudhuri, A. The physics of fluids and plasmas: An introduction for astrophysicists, New York: Cambridge University Press, 1998.

Chuychai, P. Cosmic ray acceleration at a continuous compression, Senior Project, Chulalongkorn University, 1999.

Chuychai, P., Matthaeus, W. H., and Ruffolo, D. Computer simulation of the random walk of turbulent magnetic field lines, The 7^{th} Ann. Nat. Symp. on Comp. Sci. and Eng., 2003: 110.

de Hoffmann, F., and Teller, E. Magneto-hydrodynamic shocks, Phys. Rev. **80** (1950): 692.

Earl, J. A. The effect of convection upon charged particle transport in random magnetic fields, Astrophys. J., **278** (1974): 825-840.

Foukal, P. Solar Astrophysics, New York: John Wiley & Sons, 1990.

Friedlander, M. W., Cosmic rays, Havard University Press., 1989.

Gieseler, U. D. J., Kirk, J. G., Gallent, Y. A., and Achterberg, A. Particle acceleration at oblique shocks and discontinuities of the density profile, Astron. Astrophys., **345** (1999): 298-306.

Harten, A. High resolution schemes for hyperbolic conservation laws, J. Comput. Phys. **49** (1983): 357.

Hundhausen, A. J., Coronal expansion and solar wind, Springer-Verlag, 1972.

Jackson, J. D. Classical electrodynamics, 2nd ed., John Wiley, 1975.

Kallenrode, M. B. Space physics: An introduction to plasmas and particles in the heliosphere and magnetosphere, Springer-Verlag, 2001.

Kirk, J. G., Melrose, D. B., and Priest, E. R., Plasma astrophysics, Springer-Verlag, 1994.

Klappong, K. Comparison between particle acceleration at a continuous compression and at a shock, M.Sc. Thesis, Chulalongkorn University, 2002.

Klappong, K., Leerungnavarat, K., Chuychai, P., and Ruffolo, D. Particle acceleration and pitch angle transport near a thin shock, a compression region, and a structured shock, Proc. 27^{th} Intl. Cosmic Ray Conf. (2001): 3461.

Leerungnavarat, K., Sanguansak, N., and Ruffolo, D. A hybrid orbit-finite difference method for simulating the shock acceleration of cosmic rays, The 4^{th} Ann. Nat. Symp. on Comp. Sci. and Eng., 2000.

Longair, M. S., High energy astrophysics. Volume 1: Particles, photons, and their detection, 2nd ed., Cambridge University Press, 1997.

Mewaldt, R. A., Mason, G. M., Gloeckler, G., Christian, E. R., Cohen, C. M. S., Cummings, A. C., Davis, A. J., Dwyer, J. R., Gold, R. E., Krimigis, S. M., Leske, R. A., Mazur, J. E., Stone, E. C., von Rosenvinge, T. T., Wiedenbeck, M. E., and Zurbuchen, T. H. Long-Term Fluences of Energetic Particles in the Heliosphere, AIP Conference Proceedings, **598** (2001): 165-170.

Nutaro, T., Riyavong, S., and Ruffolo, D. Application of a generalized total variation diminishing algorithm to cosmic ray transport and acceleration, Computer Physics Communications, **134** (2001): 209-222.

Parks, G. K. Physics of space plasmas: An introduction, Washington: Addison-Wesley Publishing Company, 1991.

Press, W. H., Flannery, B. P., Teukolsky, S. A., and Vetterling, W. T. Numerical Recipes in C, Cambridge University Press, 1988.

Rigden S. J. Macmillan Encyclopedia of Physics, Simon & Schuster Macmillan, 1996.

Roe, P. L. Some contributions to the modelling of discontinuous flows, in: B.E. Engquist et al. (Eds.), Proc. AMS/SIAM Sum. Sem. on Large-Scale Comp.

in Fluid Mech., 1983, Lectures in Appl. Math., **22 (2)**, Amer. Math. Soc., Providence, RI, 1985.

Ruffolo, D. Effect of adiabatic deceleration on the focused transport of solar cosmic rays, Astrophys. J., **442** (1995): 861-874.

Ruffolo, D. Transport and acceleration of energetic charged particles near an oblique shock, Astrophys. J., **515** (1999): 787-800.

Ruffolo, D. Classical mechanics, Thailand: Chulalongkorn University Press, 2002.

Ruffolo, D., and Chuychai P. First-order Fermi acceleration at a continuous compression. Proc. 26^{th} Intl. Cosmic Ray Conf., **6** (1999): 552-555.

Sanguansak, N. and Ruffolo, D. A hybrid orbit-finite difference treatment of oblique shock acceleration, Proc. 26^{th} Intl. Cosmic Ray Conf., **4** (1999): 459.

Schlickeiser, R. Cosmic ray astrophysics, Springer-Verlag, 2002.

Simpson, J. A. Elemental and isotropic composition of galactic cosmic rays, Ann. Rev. Nucl. Part. Sci., **33** (1983): 323-381.

Skilling, J. Cosmic ray streaming-I. Effect of Alfvén wave on particles, Mon. Not. R. Astr. Soc., **172** (1975): 557-566.

Sweby, P. K. High resolution schemes using flux limiter for hyperbolic conservation law, SIAM Numer. Anual., **21** (1984): 995.

Terasawa, T. Energy spectrum and pitch angle distribution of particles reflected by MHD shock waves of fast mode, Planet. Space Sci., **27** (1979): 193-201.

Appendices

Appendix A

$n(p)$ vs. $j(E)$ and γ vs. γ_E

A.1 $n(p)$ vs. $j(E)$

Here we will show that the quantities $n(p)$ and $j(E)$, introduced in Chapter 2, are equivalent. Recall the definition of $n(p)$ as particle number/(volume · solid angle · momentum/nucleon):

$$n(p) = \frac{d^6N}{dxdydzdpd\Omega}, \tag{A.1}$$

where N is the number of particles, x, y, and z are the spatial coordinates, p is the momentum/nucleon of particles, and Ω is the solid angle. If we multiply equation (A.1) by dE/dE, where E is the kinetic energy/nucleon of particles. We obtain

$$n(p) = \frac{d^6N}{dxdydzdEd\Omega} \cdot \frac{dE}{dp}. \tag{A.2}$$

Referring to the relation

$$E_{\text{total}}^2 = p^2c^2 + m^2c^4, \tag{A.3}$$

where E_{total} is the total energy of a particle, m is the rest mass, and c is the speed of light, by differentiating equation (A.3), it becomes

$$2E_{\text{total}}dE_{\text{total}} = 2pdp \cdot c^2. \tag{A.4}$$

Then we can find dE_{total}/dp,

$$\frac{dE_{\text{total}}}{dp} = \frac{pc^2}{E_{\text{total}}}$$

$$= \frac{\gamma m v c^2}{\gamma m c^2}$$
$$= v, \tag{A.5}$$

where γ is the Lorentz factor of a particle and v is the particle speed. From the relation

$$E_{\text{total}} = E + mc^2, \tag{A.6}$$

dE is equal to dE_{total}. Hence dE/dp is also equal to v. When dE/dp is substituted into equation (A.2), we obtain

$$\begin{aligned} n(p) &= v \cdot \frac{d^6N}{dxdydzdEd\Omega} \\ &= \frac{d^6N}{dtdAdEd\Omega}, \end{aligned} \tag{A.7}$$

where t is the time and A is the area of interest. This is the particle flux in terms of energy. As discussed in §2.1.2, this is $j(E)$. Therefore $n(p)$ is the same as $j(E)$.

A.2 γ vs. γ_E

Recalling that

$$E_{\text{total}} = \sqrt{m^2c^4 + p^2c^2}, \tag{A.8}$$

where E_{total} is the total energy of a particle, in non-relativistic limit we can approximate (keeping the first two terms in the binomial expansion) that

$$\begin{aligned} E_{\text{total}} &\approx mc^2\left(1 + \frac{1}{2}\frac{p^2c^2}{m^2c^4}\right) \\ &\approx mc^2 + \frac{p^2}{2m}. \end{aligned} \tag{A.9}$$

Since mc^2 is the particle rest energy, the particle kinetic energy is $E \approx p^2/2m$.

From the relation describing the cosmic ray spectrum,

$$j(E) \propto E^{-\gamma_e} \tag{A.10}$$

together with $E \propto p^2$, we get

$$j(p) \propto p^{-2\gamma_e}. \tag{A.11}$$

Recalling that the exponent of the momentum p is defined as $-\gamma$, therefore, in the non-relativistic limit, $\gamma = 2\gamma_e$.

In the ultrarelativistic limit, the term m^2c^4 is very small compared with the term p^2c^2. We can approximate that

$$E \approx pc. \tag{A.12}$$

Then E is proportional to p. Therefore, in the ultrarelativistic limit, γ should be equal to γ_e.

Appendix B
Origin of GCR: Supernova Shocks

Here are some relevant observations supporting that galactic cosmic rays are accelerated at supernova shocks.

1. Supernovae are the only known, ongoing phenomena in the galaxy that can provide the energy input rate required to continually replenish the energy of GCR.

2. Supernova remnants show evidence of shock (e.g., as observed by the *Hubble Space Telescope*).

3. Supernova remnants show evidence of shock acceleration of electrons (as evidence by radio observations of synchrotron radiation).

4. The primary GCR abundances are similar to solar system abundances. [More precisely, when correcting for galactic propagation, the inferred "cosmic ray source" elemental abundances are similar to solar system abundance.]

5. The solar system provides a sample of matter in the galaxy, i.e., the interstellar medium (ISM), 4.56 billion years ago. Therefore, the similarity of cosmic ray source abundances to solar system abundances may indicate an origin in the ISM.

6. The cosmic ray source elemental abundances are lower than solar system abundances by a factor of three for elements with a high first ionization potential (greater than about 8 eV). This is most easily explained by a "cool" source at a temperature of about 10^5 K (so that $kT \sim 8$ eV). [Note: there are

alternative interpretations of the correlation with the first ionization potential - however, all proposed models agree on acceleration by supernova shocks.]

7. Recent observations of primary GCR that decay only by electron capture indicate a time of at least 10^4 years between nucleosynthesis and acceleration.

Several of these observations are inconsistent with direct acceleration during a supernova event. [One more (theoretical) point is that during, the expansion of the supernova ejecta, adiabatic deceleration would rapidly reduce the particles' energy.] On the other hand, all these observations point to or are consistent with acceleration by supernova shocks propagating through the ISM.

Appendix B is taken from a lecture document on Cosmic Rays of Assoc. Prof. Dr. David Ruffolo.

Appendix C
Simulation Parameters

	Q-Par	Ob	Q-Perp
tan(THETAup)	0.01	1	4
tan(THETAdown)	0.04	3.87	15.11
THETAup (radian)	0.009999667	0.785398163	1.325817664
THETAdown (radian)	0.039978687	1.318242051	1.504711361
THETAup (degree)	0.572938698	45	75.96375652
THETAdown (degree)	2.290610042	75.52970589	86.21361035
BDOVERBU	1.001	2.83	3.673
vsw_up(km/s) (normal-incidence frame)	537.981	541.458	544.271
vsw_down(km/s) (normal-incidence frame)	137.981	141.458	144.271
BETASW_up (normal-incidence frame)	0.001795099	0.0018067	0.001816087
BETASW_down (normal-incidence frame)	0.000460406	0.000472007	0.000481394
vsw_up(km/s) (de Hoffmann-Teller frame)	538.0078984	765.7372471	2244.086822
vsw_down(km/s) (de Hoffmann-Teller frame)	138.0913407	566.1082177	2184.703618
BETASW_up (de Hoffmann-Teller frame)	0.001795188	0.00255506	0.007487917
BETASW_down (de Hoffmann-Teller frame)	0.000460774	0.001888952	0.007289771

Table C.1: Simulation parameters for various field angles

Q-Perp

#momentum	9	8	7	6	5	4	3	2	1	0	fluid-farup
beta	0.09988	0.0908	0.08172	0.07264	0.06356	0.05448	**0.0454**	0.03632	0.02724	0.01816	0.001816
v/u1n	55	50	45	40	35	30	**25**	20	15	10	1
gamma (Lorentz factor)	1.005026	1.004148	1.003356	1.002649	1.002026	1.001487	**1.001032**	1.00066	1.000371	1.000165	1.000002
p (MeV/c)	94.18639	85.54922	76.93356	68.33719	59.75791	51.19352	**42.64188**	34.10083	25.56824	17.04198	1.703919
energy (MeV)	4.715458	3.891973	3.148771	2.48529	1.901028	1.395548	**0.96847**	0.619475	0.348304	0.154754	0.001547
delt (upstream)	0.224149	0.246706	0.274262	0.308689	0.352933	0.411903	0.494433	0.618194	0.824417	1.236796	12.3693
ln<j>/z (upstream)	-0.92727	-1.02	-1.13333	-1.275	-1.45714	-1.7	-2.04	-2.55	-3.4	-5.1	-51

Table C.2: Simulation parameters for various momenta in the case of a quasi-perpendicular magnetic field

Oblique

#momentum	9	8	7	6	5	4	3	2	1	0	fluid-farup
beta	0.099385	0.09035	0.081315	0.07228	0.063245	0.05421	0.045175	0.03614	0.027105	0.01807	0.001807
v/u1n	55	50	45	40	35	30	25	20	15	10	1
gamma (Lorentz factor)	1.004976	1.004107	1.003323	1.002622	1.002006	1.001473	1.001022	1.000654	1.000368	1.000163	1.000002
p (MeV/c)	93.71494	85.12174	76.54974	67.99673	59.46056	50.93906	42.43012	33.93161	25.44143	16.95749	1.695475
energy (MeV)	4.668486	3.853254	3.117483	2.46062	1.882175	1.381719	0.95888	0.613344	0.344858	0.153223	0.001532
delt (upstream)	0.076885	0.084622	0.094073	0.105881	0.121057	0.141283	0.16959	0.21204	0.282773	0.424218	4.242636
ln<j>/z (upstream)	-0.10909	-0.12	-0.13333	-0.15	-0.17143	-0.2	-0.24	-0.3	-0.4	-0.6	-6

Table C.3: Simulation parameters for various momenta in the case of an oblique magnetic field

Q-Par

#momentum	9	8	7	6	5	4	3	2	1	0	fluid-farup
beta	0.098725	0.08975	0.030775	0.0718	0.062825	0.05385	0.044875	0.0359	0.026925	0.01795	0.001795
v/u1n	55	50	45	40	35	30	25	20	15	10	1
gamma (Lorentz factor	1.004909	1.004052	1.003278	1.002588	1.001979	1.001453	1.001008	1.000645	1.000363	1.000161	1.000002
p (MeV/c)	93.08644	84.55185	76.03803	67.54283	59.06412	50.5998	42.14777	33.70598	25.27235	16.84484	1.684215
energy (MeV)	4.606231	3.801936	3.076012	2.427921	1.857186	1.363389	0.946167	0.605217	0.340291	0.151195	0.001512
delt (upstream)	0.054371	0.059842	0.066525	0.074875	0.085606	0.099908	0.119925	0.149943	0.199962	0.299983	3.000147
ln<j>/z (upstream)	-0.05455	-0.06001	-0.06667	-0.07501	-0.08572	-0.10001	-0.12001	-0.15002	-0.20002	-0.30003	-3.0003

Table C.4: Simulation parameters for various momenta in the case of a quasi-parallel magnetic field

Appendix D
All Results

Appendix D provides all results obtained by solving the pitch-angle transport equation with a finite-difference method and solving the diffusion-convection equation with a shooting method, consisting of the spatial distribution of particles ($\langle j \rangle_\mu$ vs. $z/\lambda_\parallel$), particle spectrum ($\log\langle j \rangle_1$ vs. $\log(p)$), spectral index (γ), spectral index as a function of compression width (γ vs. $b/\lambda_\parallel$), upstream-density decay rate ($\ln\langle j \rangle$ vs. $(z/\lambda_\parallel)$), and particle anisotropy as a function of position (δ vs. $z/\lambda_\parallel$).

The spatial distribution of particles is shown in §D.1. The distributions yielded by the pitch-angle transport and diffusion-convection equations are plotted on the same graphs for easy comparison. Plots of the particle spectrum are shown in §D.2 (only for pitch-angle transport). Spectral indices for every case of interest are summarized in a table in §D.3. The spectral index is plotted as a function of compression width in §D.4. In §D.5 and §D.6, the upstream-density decay rate and anisotropy of particles, respectively, for pitch-angle transport are plotted as functions of position. The decay rate and anisotropy are used to check our results by comparing them with the analytically calculated decay rate and anisotropy far downstream, shown in Appendix C.

D.1 $\langle j \rangle_\mu$ vs. $z/\lambda_\parallel$

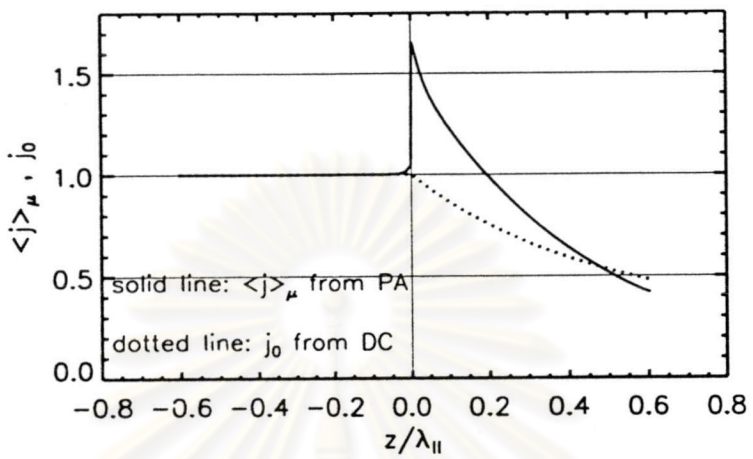

Figure D.1: $\langle j \rangle_\mu$ vs. $z/\lambda_\parallel$ of a quasi-perpendicular shock, v/U_{1n}=25

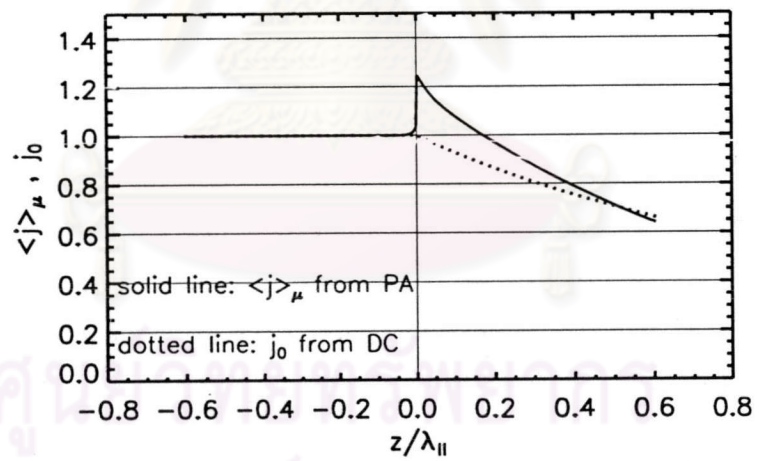

Figure D.2: $\langle j \rangle_\mu$ vs. $z/\lambda_\parallel$ of a quasi-perpendicular shock, v/U_{1n}=50

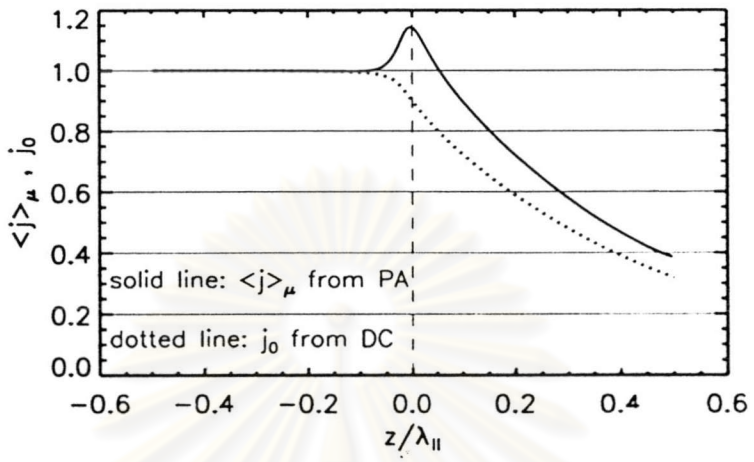

Figure D.3: $\langle j \rangle_\mu$ vs. $z/\lambda_\parallel$ of a quasi-perpendicular compression region with $b/\lambda_\parallel = 0.2$, v/U_{1n}=25

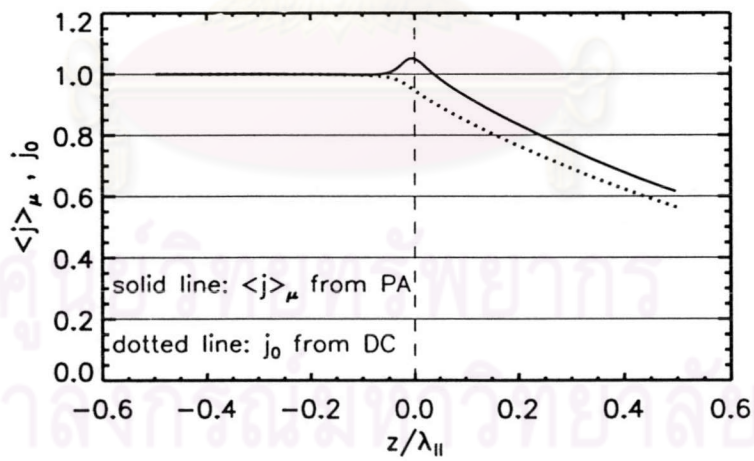

Figure D.4: $\langle j \rangle_\mu$ vs. $z/\lambda_\parallel$ of a quasi-perpendicular compression region with $b/\lambda_\parallel = 0.2$, v/U_{1n}=50

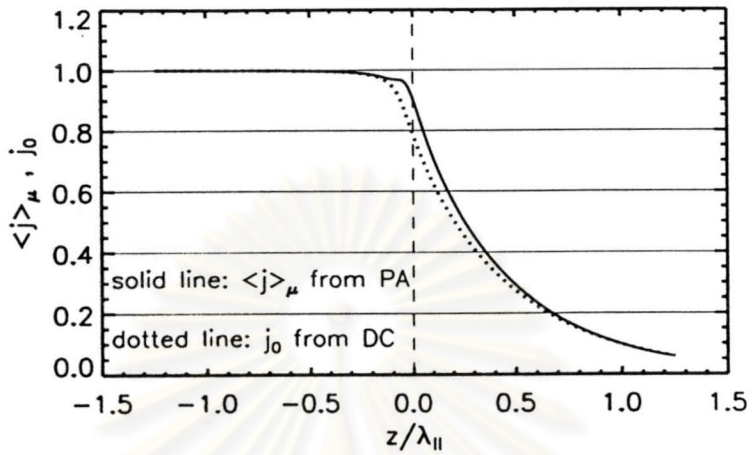

Figure D.5: $\langle j \rangle_\mu$ vs. $z/\lambda_\parallel$ of a quasi-perpendicular compression region with $b/\lambda_\parallel = 0.5$, v/U_{1n}=25

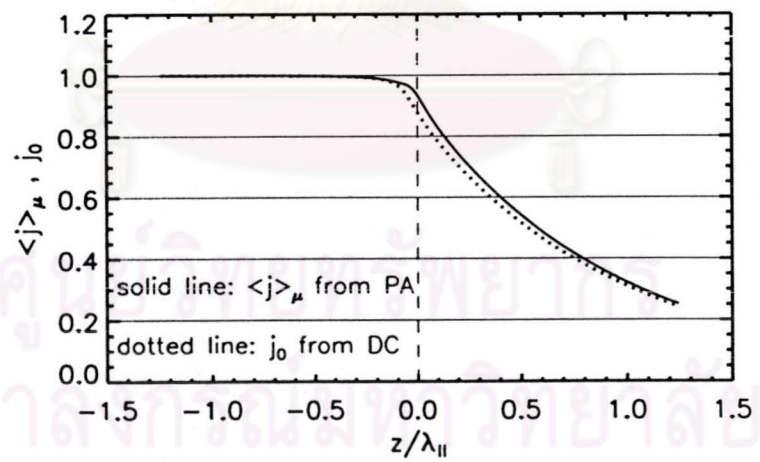

Figure D.6: $\langle j \rangle_\mu$ vs. $z/\lambda_\parallel$ of a quasi-perpendicular compression region with $b/\lambda_\parallel = 0.5$, v/U_{1n}=50

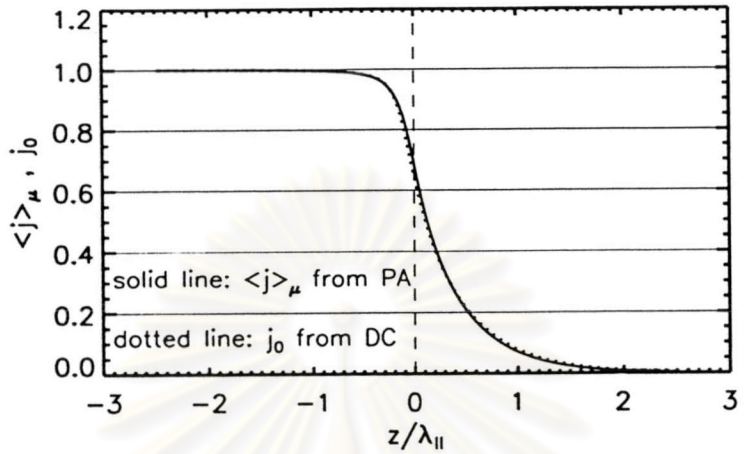

Figure D.7: $\langle j \rangle_\mu$ vs. $z/\lambda_\parallel$ of a quasi-perpendicular compression region with $b/\lambda_\parallel = 1.0$, v/U_{1n}=25

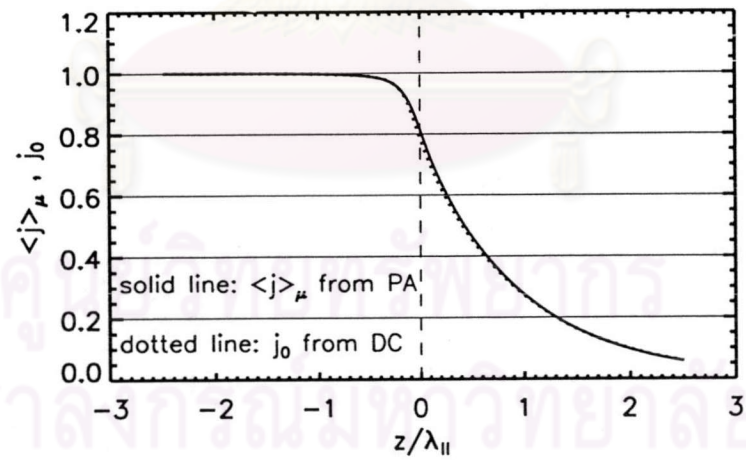

Figure D.8: $\langle j \rangle_\mu$ vs. $z/\lambda_\parallel$ of a quasi-perpendicular compression region with $b/\lambda_\parallel = 1.0$, v/U_{1n}=50

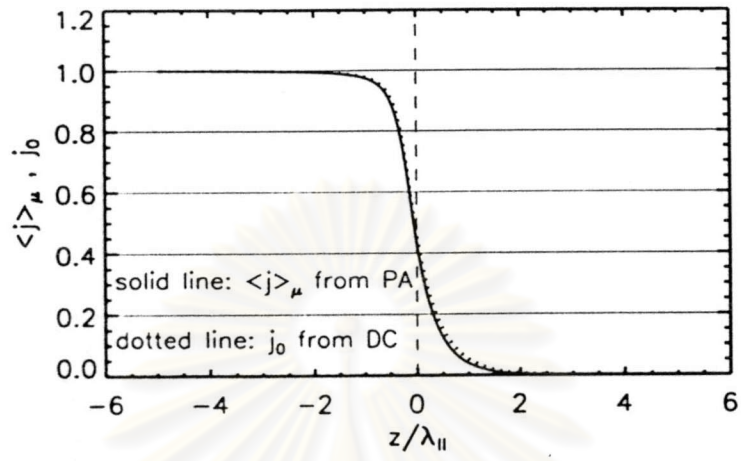

Figure D.9: $\langle j \rangle_\mu$ vs. $z/\lambda_\parallel$ of a quasi-perpendicular compression region with $b/\lambda_\parallel = 2.0$, v/U_{1n}=25

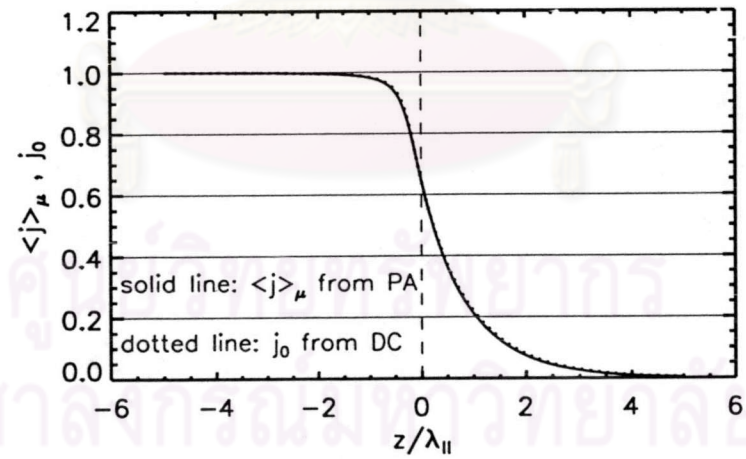

Figure D.10: $\langle j \rangle_\mu$ vs. $z/\lambda_\parallel$ of a quasi-perpendicular compression region with $b/\lambda_\parallel = 2.0$, v/U_{1n}=50

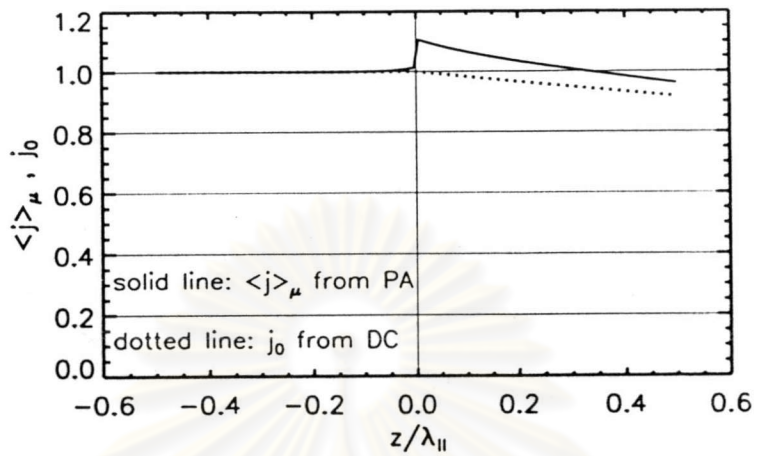

Figure D.11: $\langle j \rangle_\mu$ vs. $z/\lambda_\parallel$ of an oblique shock, v/U_{1n}=25

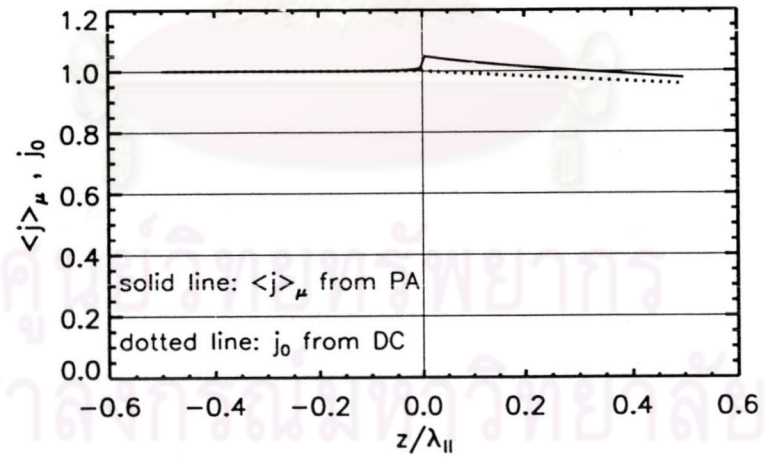

Figure D.12: $\langle j \rangle_\mu$ vs. $z/\lambda_\parallel$ of an oblique shock, v/U_{1n}=50

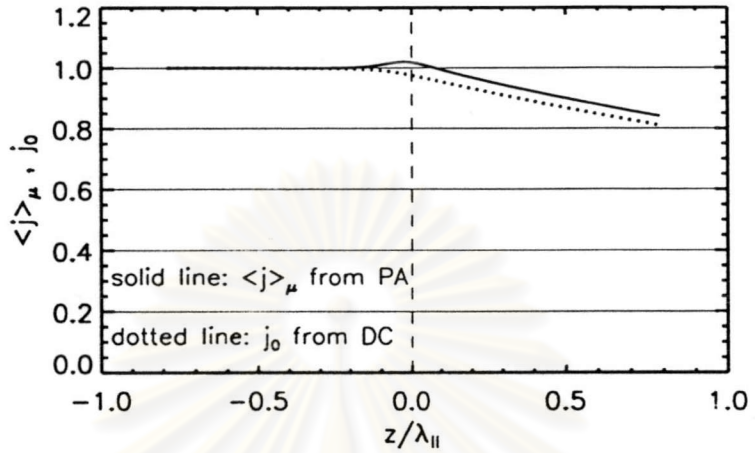

Figure D.13: $\langle j \rangle_\mu$ vs. $z/\lambda_\parallel$ of an oblique compression region with $b/\lambda_\parallel = 0.2$, v/U_{1n}=25

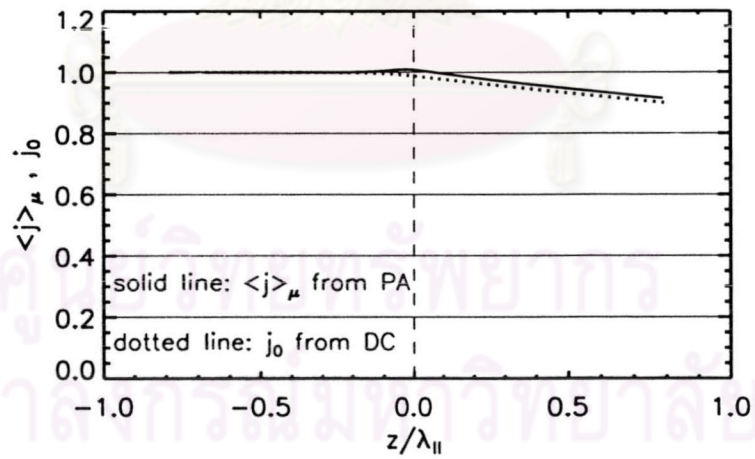

Figure D.14: $\langle j \rangle_\mu$ vs. $z/\lambda_\parallel$ of an oblique compression region with $b/\lambda_\parallel = 0.2$, v/U_{1n}=50

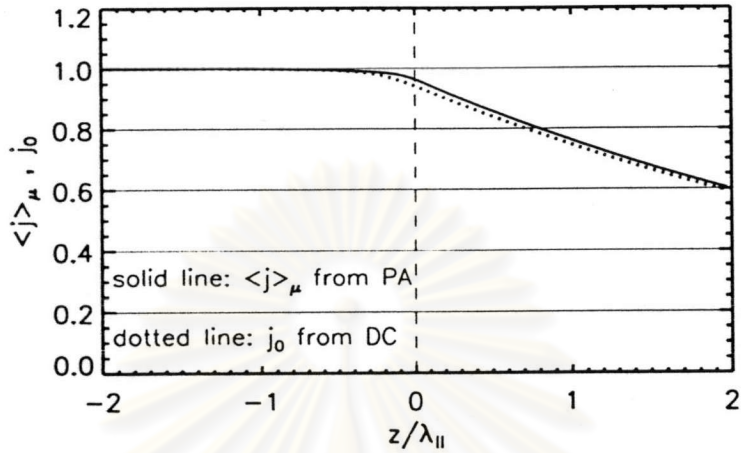

Figure D.15: $\langle j \rangle_\mu$ vs. $z/\lambda_\parallel$ of an oblique compression region with $b/\lambda_\parallel = 0.5$, v/U_{1n}=25

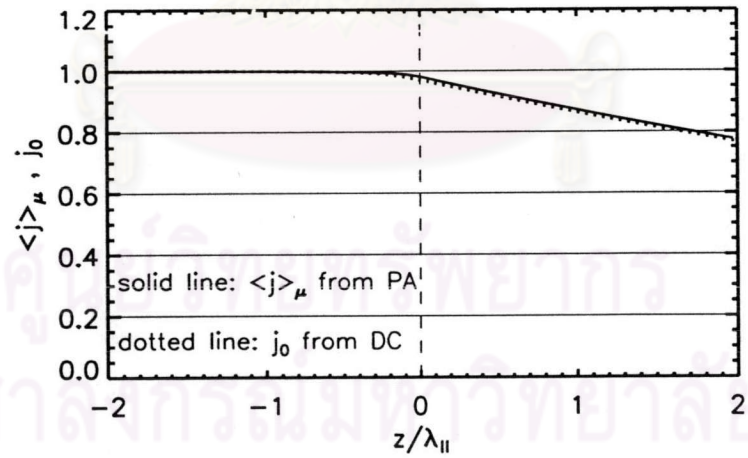

Figure D.16: $\langle j \rangle_\mu$ vs. $z/\lambda_\parallel$ of an oblique compression region with $b/\lambda_\parallel = 0.5$, v/U_{1n}=50

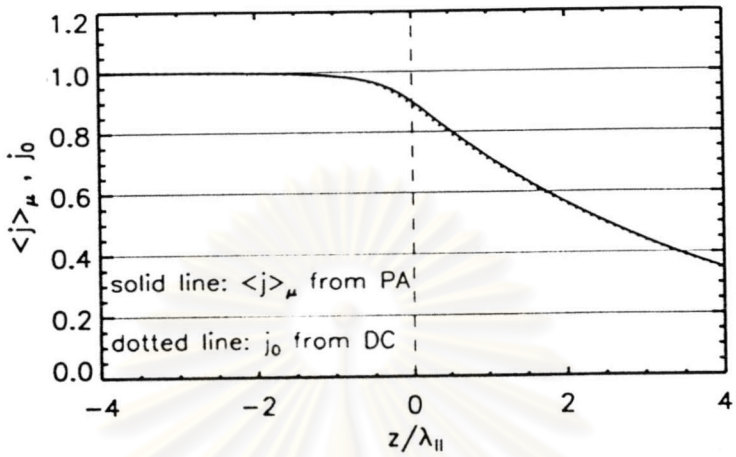

Figure D.17: $\langle j \rangle_\mu$ vs. $z/\lambda_{\|}$ of an oblique compression region with $b/\lambda_{\|} = 1.0$, v/U_{1n}=25

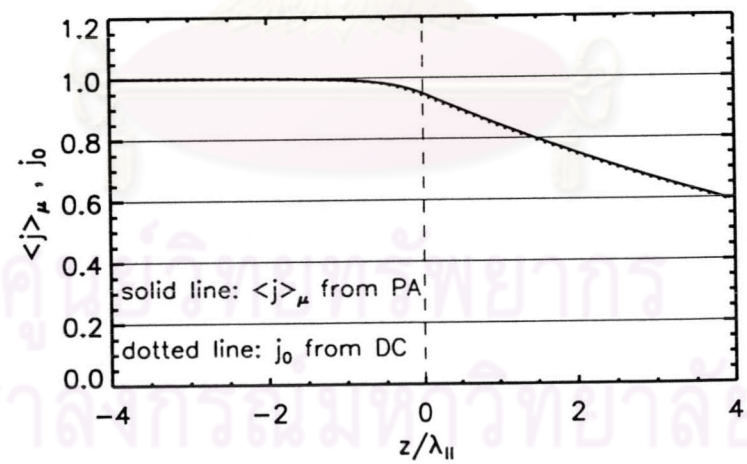

Figure D.18: $\langle j \rangle_\mu$ vs. $z/\lambda_{\|}$ of an oblique compression region with $b/\lambda_{\|} = 1.0$, v/U_{1n}=50

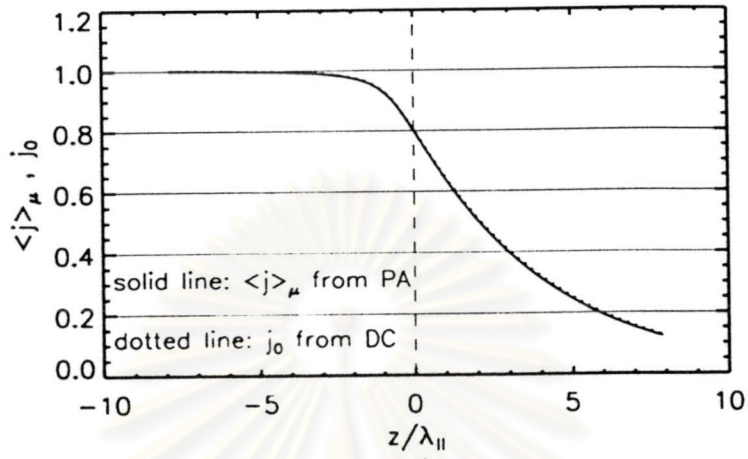

Figure D.19: $\langle j \rangle_\mu$ vs. $z/\lambda_\parallel$ of an oblique compression region with $b/\lambda_\parallel = 2.0$, v/U_{1n}=25

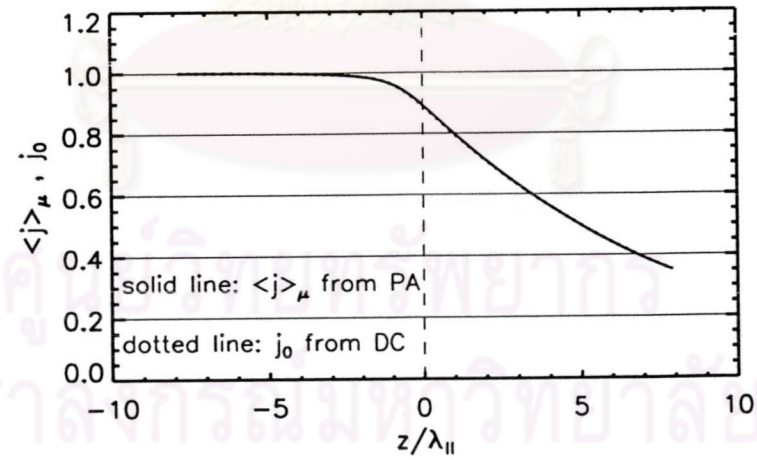

Figure D.20: $\langle j \rangle_\mu$ vs. $z/\lambda_\parallel$ of an oblique compression region with $b/\lambda_\parallel = 2.0$, v/U_{1n}=50

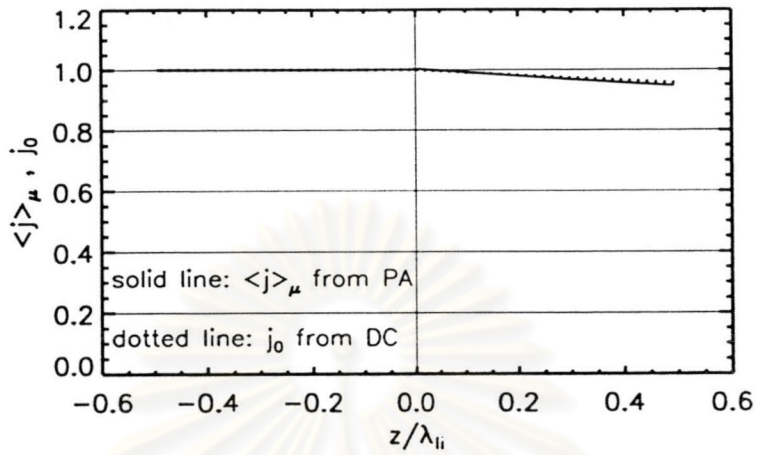

Figure D.21: $\langle j \rangle_\mu$ vs. $z/\lambda_\parallel$ of a quasi-parallel shock, v/U_{1n}=25

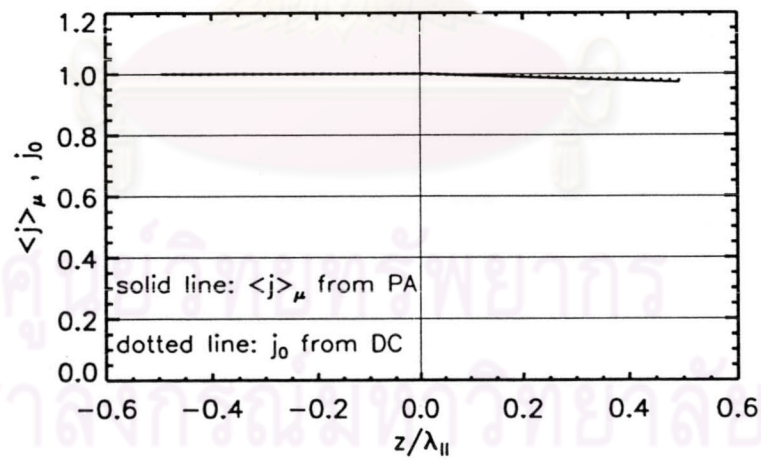

Figure D.22: $\langle j \rangle_\mu$ vs. $z/\lambda_\parallel$ of a quasi-parallel shock, v/U_{1n}=50

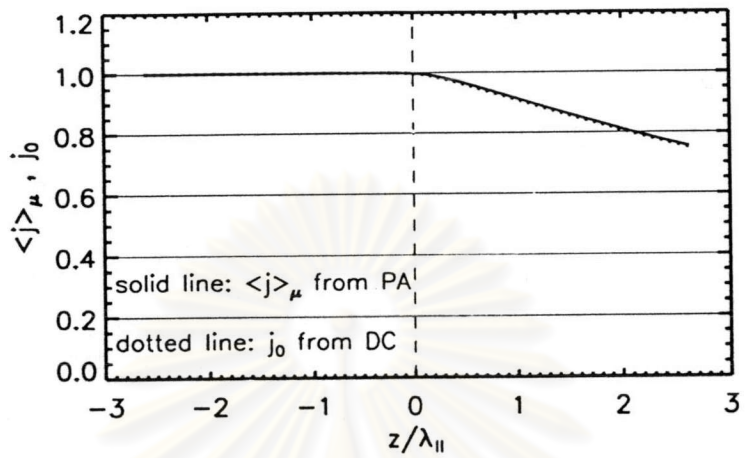

Figure D.23: $\langle j \rangle_\mu$ vs. $z/\lambda_\parallel$ of a quasi-parallel compression region with $b/\lambda_\parallel = 0.2$, v/U_{1n}=25

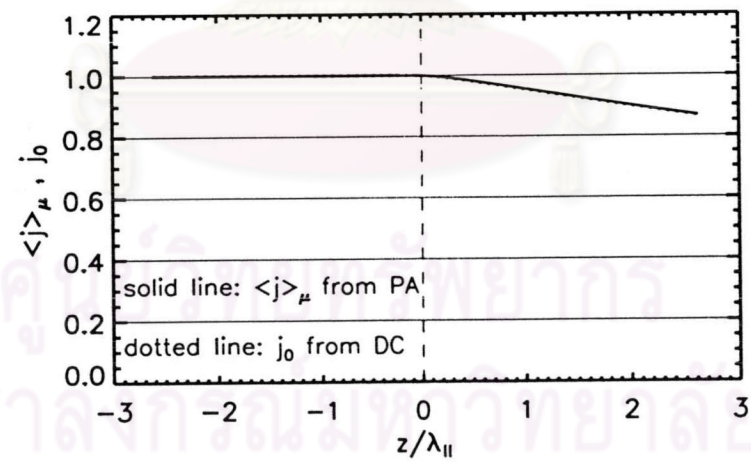

Figure D.24: $\langle j \rangle_\mu$ vs. $z/\lambda_\parallel$ of a quasi-parallel compression region with $b/\lambda_\parallel = 0.2$, v/U_{1n}=50

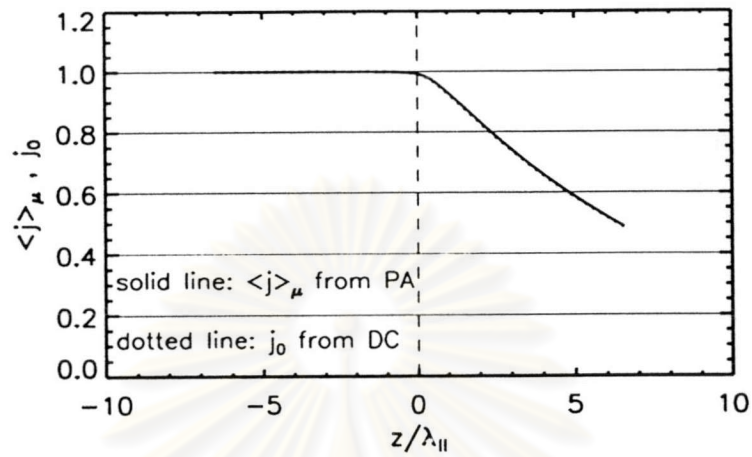

Figure D.25: $\langle j \rangle_\mu$ vs. $z/\lambda_\parallel$ of a quasi-parallel compression region with $b/\lambda_\parallel = 0.5$, v/U_{1n}=25

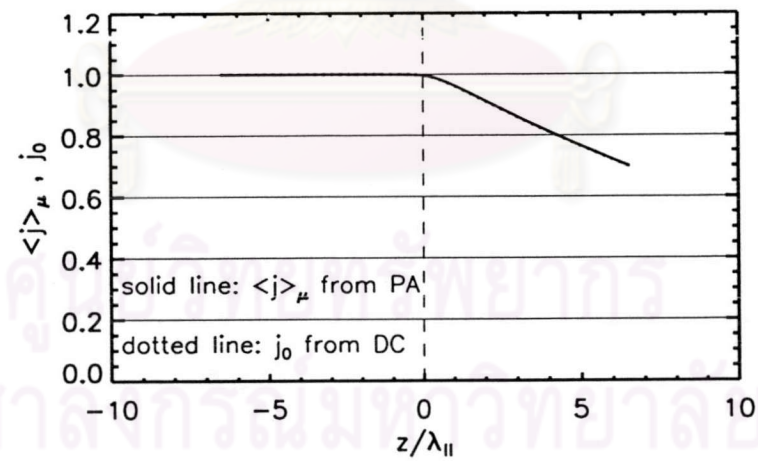

Figure D.26: $\langle j \rangle_\mu$ vs. $z/\lambda_\parallel$ of a quasi-parallel compression region with $b/\lambda_\parallel = 0.5$, v/U_{1n}=50

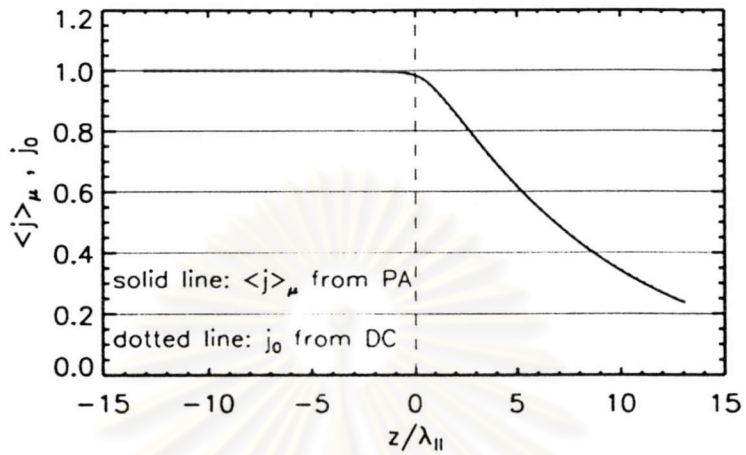

Figure D.27: $\langle j \rangle_\mu$ vs. $z/\lambda_\parallel$ of a quasi-parallel compression region with $b/\lambda_\parallel = 1.0$, v/U_{1n}=25

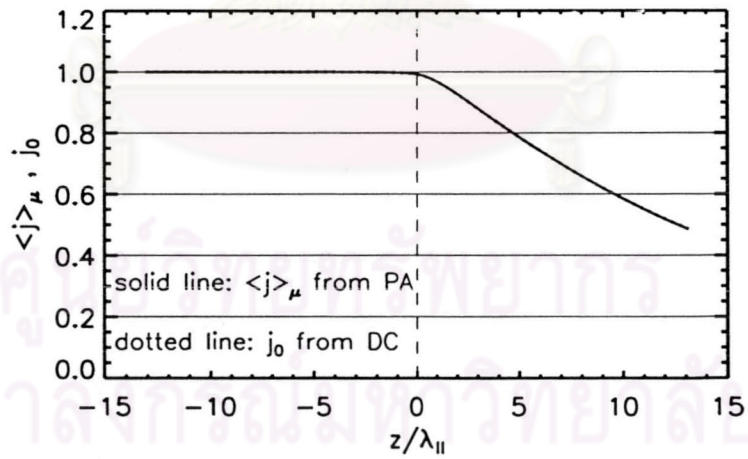

Figure D.28: $\langle j \rangle_\mu$ vs. $z/\lambda_\parallel$ of a quasi-parallel compression region with $b/\lambda_\parallel = 1.0$, v/U_{1n}=50

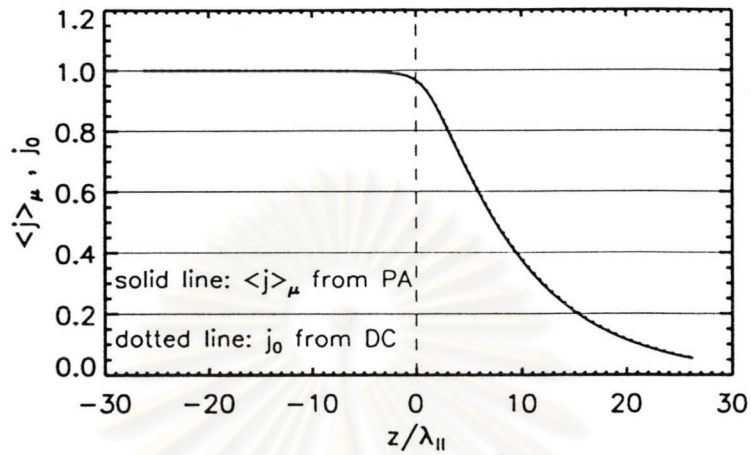

Figure D.29: $\langle j \rangle_\mu$ vs. $z/\lambda_\parallel$ of a quasi-parallel compression region with $b/\lambda_\parallel = 2.0$, v/U_{1n}=25

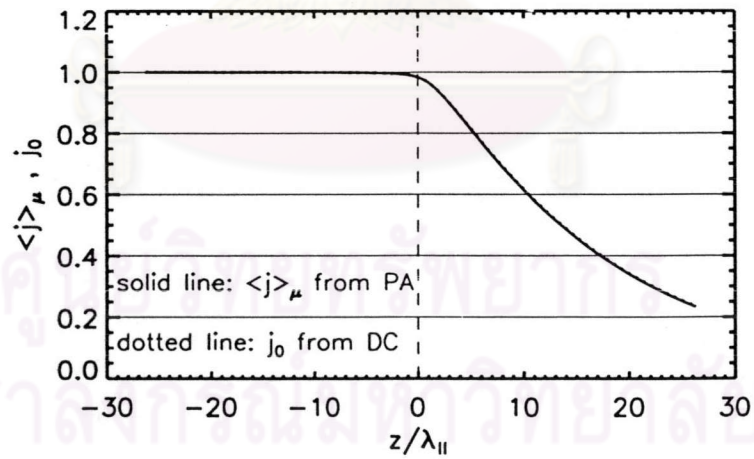

Figure D.30: $\langle j \rangle_\mu$ vs. $z/\lambda_\parallel$ of a quasi-parallel compression region with $b/\lambda_\parallel = 2.0$, v/U_{1n}=50

D.2 $\log\langle j\rangle_1$ vs. $\log(p)$

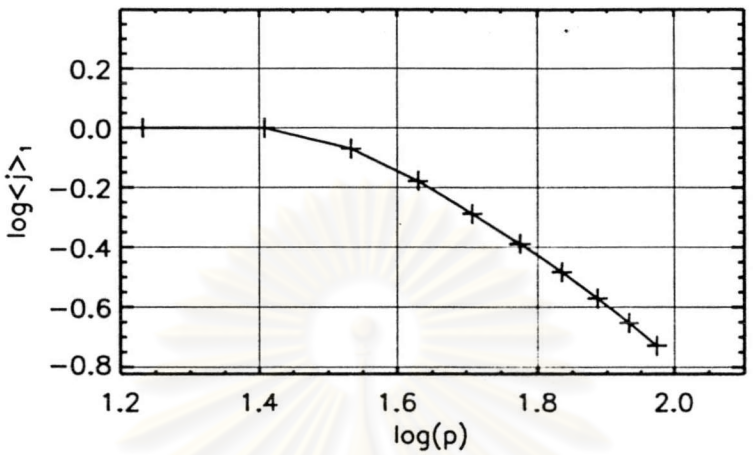

Figure D.31: $\log\langle j\rangle_1$ vs. $\log(p)$ of a quasi-perpendicular shock obtained by the pitch-angle transport equation

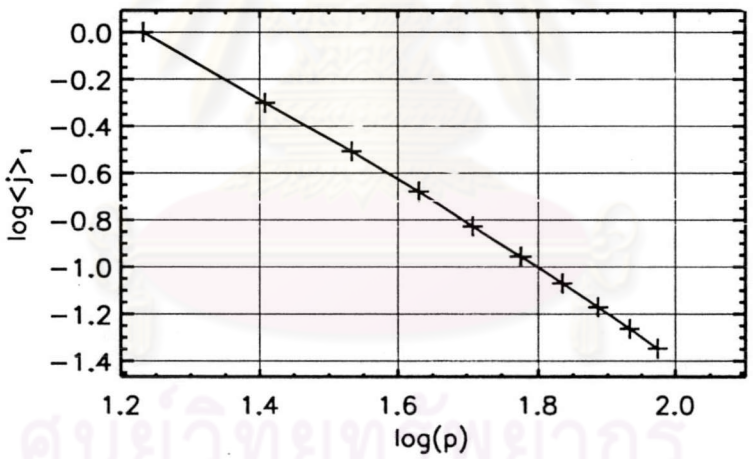

Figure D.32: $\log\langle j\rangle_1$ vs. $\log(p)$ of a quasi-perpendicular compression region with $b/\lambda_{\parallel} = 0.2$ obtained by the pitch-angle transport equation

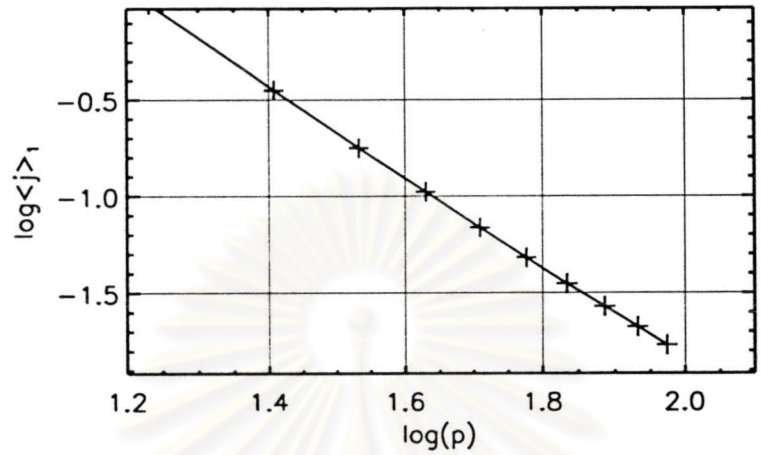

Figure D.33: $\log\langle j\rangle_1$ vs. $\log(p)$ of a quasi-perpendicular compression region with $b/\lambda_{\|} = 0.5$ obtained by the pitch-angle transport equation

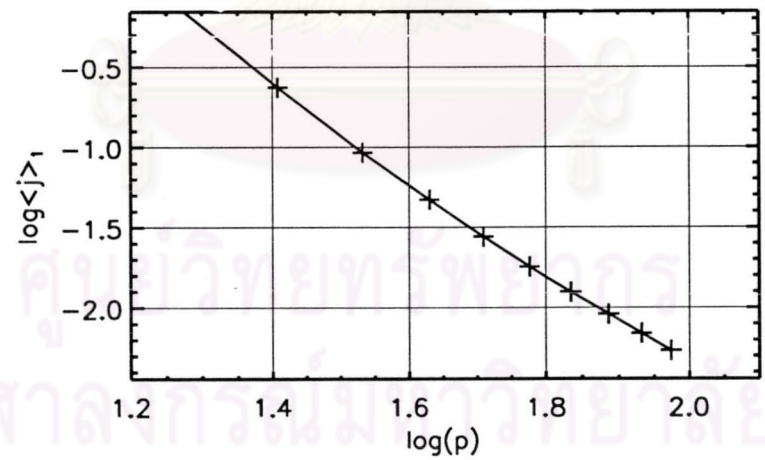

Figure D.34: $\log\langle j\rangle_1$ vs. $\log(p)$ of a quasi-perpendicular compression region with $b/\lambda_{\|} = 1.0$ obtained by the pitch-angle transport equation

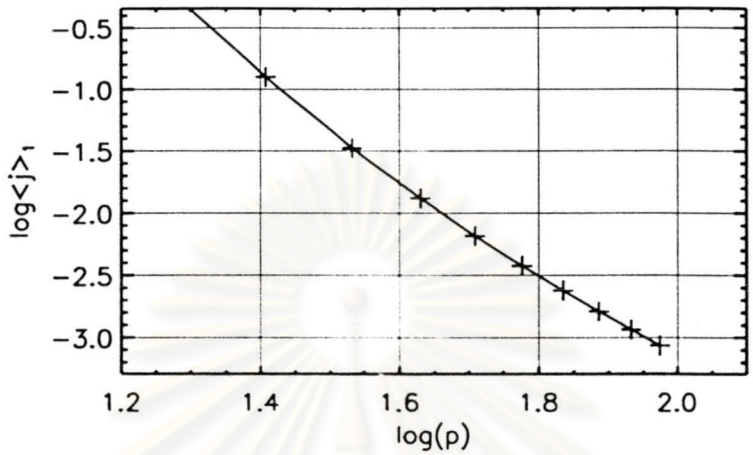

Figure D.35: $\log\langle j\rangle_1$ vs. $\log(p)$ of a quasi-perpendicular compression region with $b/\lambda_{\parallel} = 2.0$ obtained by the pitch-angle transport equation

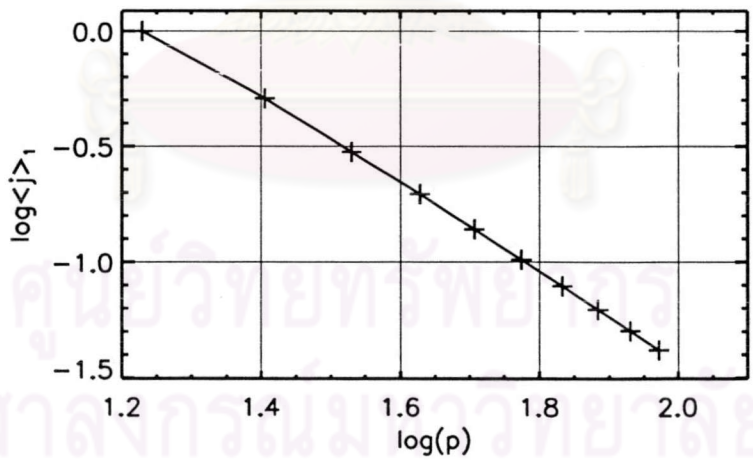

Figure D.36: $\log\langle j\rangle_1$ vs. $\log(p)$ of an oblique shock obtained by the pitch-angle transport equation

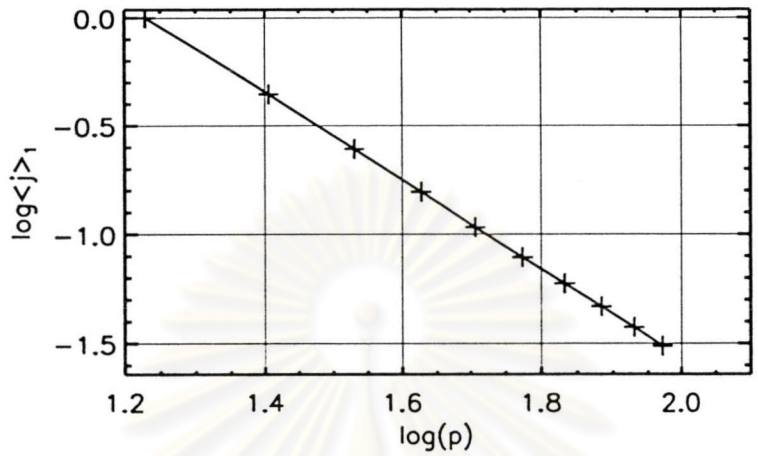

Figure D.37: $\log\langle j\rangle_1$ vs. $\log(p)$ of an oblique compression region with $b/\lambda_{||} = 0.2$ obtained by the pitch-angle transport equation

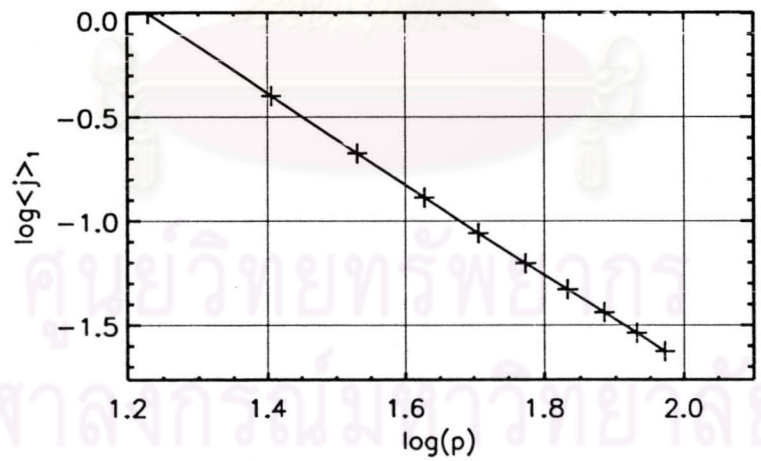

Figure D.38: $\log\langle j\rangle_1$ vs. $\log(p)$ of an oblique compression region with $b/\lambda_{||} = 0.5$ obtained by the pitch-angle transport equation

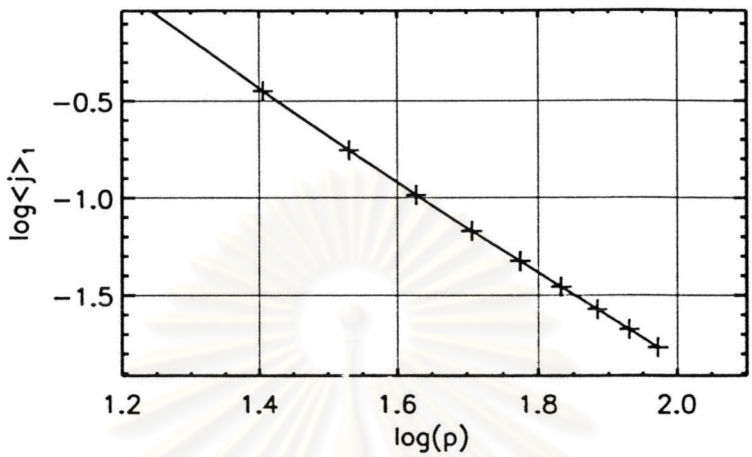

Figure D.39: $\log\langle j\rangle_1$ vs. $\log(p)$ of an oblique compression region with $b/\lambda_{\|} = 1.0$ obtained by the pitch-angle transport equation

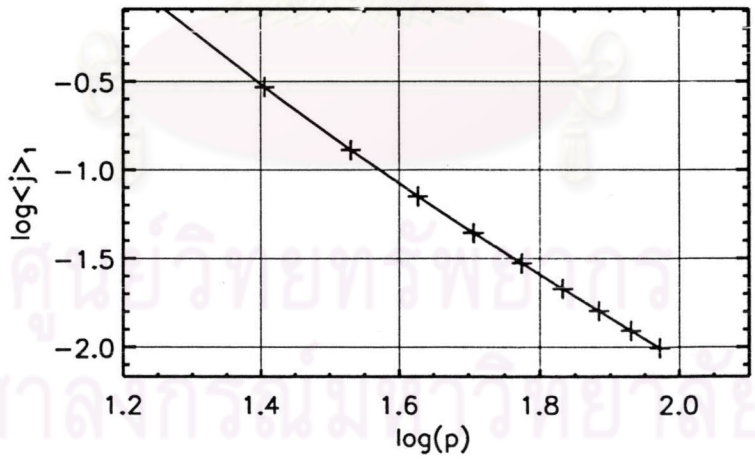

Figure D.40: $\log\langle j\rangle_1$ vs. $\log(p)$ of an oblique compression region with $b/\lambda_{\|} = 2.0$ obtained by the pitch-angle transport equation

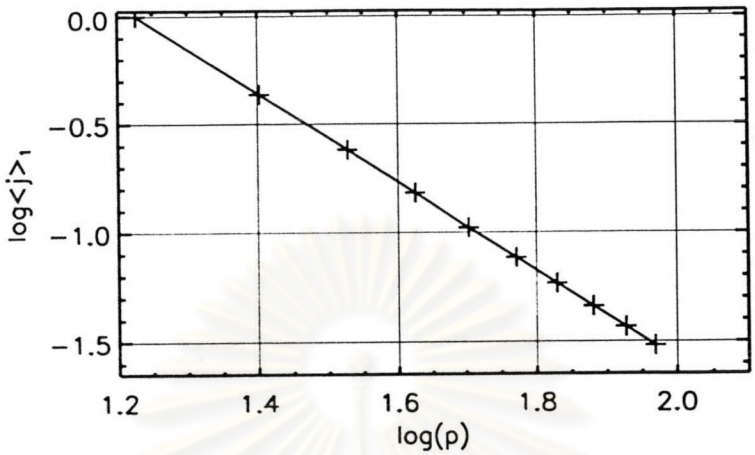

Figure D.41: $\log\langle j\rangle_1$ vs. $\log(p)$ of a quasi-parallel shock obtained by the pitch-angle transport equation

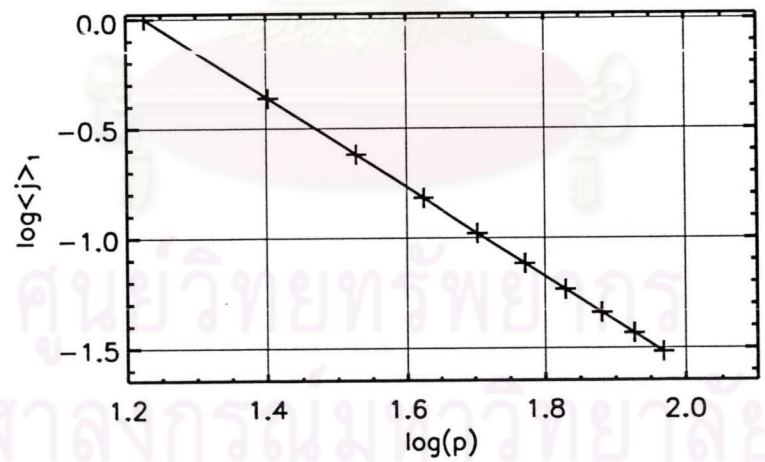

Figure D.42: $\log\langle j\rangle_1$ vs. $\log(p)$ of a quasi-parallel compression region with $b/\lambda_{\parallel} = 0.2$ obtained by the pitch-angle transport equation

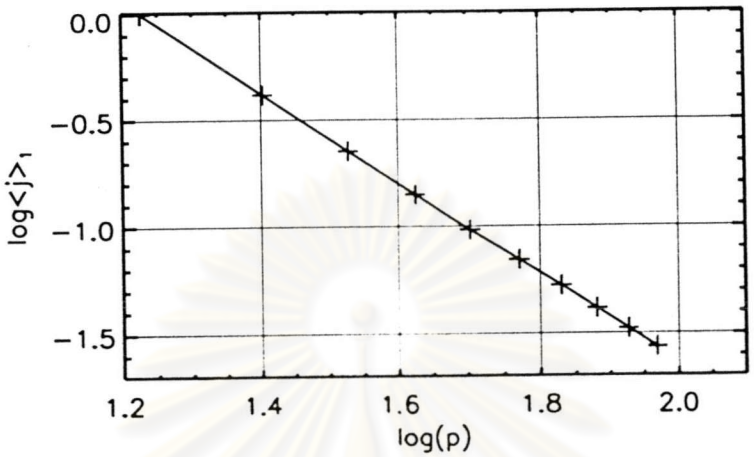

Figure D.43: $\log\langle j\rangle_1$ vs. $\log(p)$ of a quasi-parallel compression region with $b/\lambda_{\|} = 0.5$ obtained by the pitch-angle transport equation

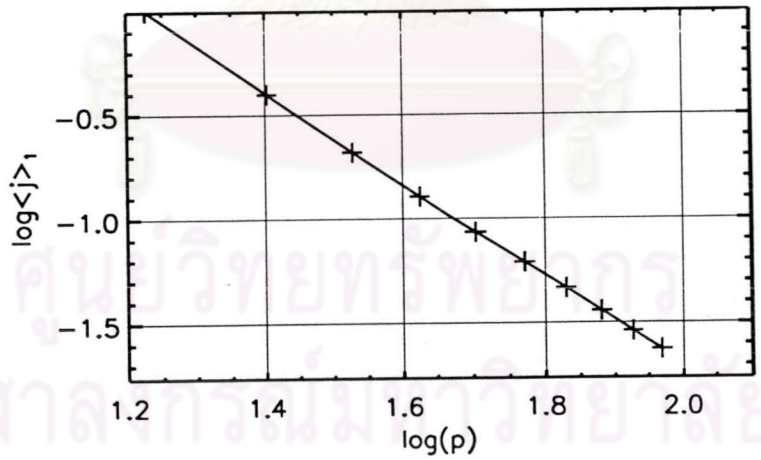

Figure D.44: $\log\langle j\rangle_1$ vs. $\log(p)$ of a quasi-parallel compression region with $b/\lambda_{\|} = 1.0$ obtained by the pitch-angle transport equation

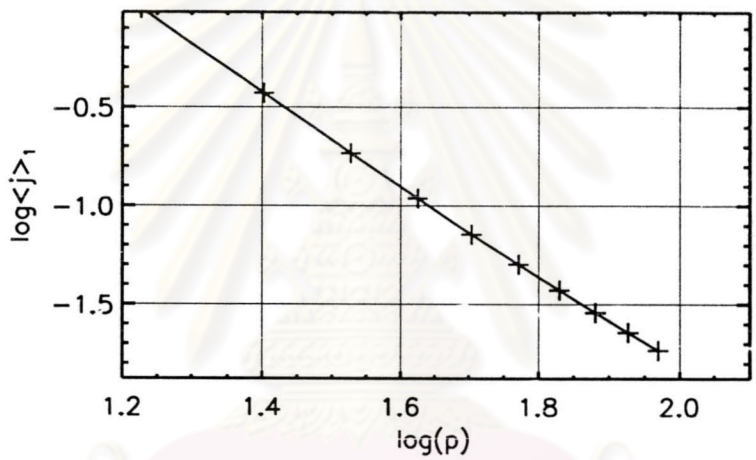

Figure D.45: $\log\langle j\rangle_1$ vs. $\log(p)$ of a quasi-parallel compression region with $b/\lambda_{\parallel} = 2.0$ obtained by the pitch-angle transport equation

D.3 Spectral Index Summary

Summary Chart		Q-Perp(Ob2)			Ob			Q-Par		
		eq-0.3	eq	eq+0.3	eq-0.3	eq	eq+0.3	eq-0.3	eq	eq+0.3
shock	gamma_p	-0.25	0.05	0.35	1.39	1.69	1.99	1.61	1.91	2.21
	gamma_f25	1.234	1.230	n/a	1.896	1.896	1.896	2.043	2.043	2.043
	gam_dc25	---------	2.081	---------	---------	2.061	---------	---------	2.034	---------
	gamma_f50	1.790	1.790	n/a	1.991	1.992	1.993	2.039	2.040	2.042
	gam_dc50	---------	2.081	---------	---------	2.061	---------	---------	2.034	---------
0.2	gamma_p	1.47	1.77	2.07	1.73	2.03	2.33	1.75	2.05	2.35
	gamma_f25	1.814	1.809	1.805	2.042	2.042	2.043	2.040	2.041	2.043
	gam_dc25	---------	2.226	---------	---------	2.096	---------	---------	2.027	---------
	gamma_f50	2.000	2.000	2.000	2.054	2.056	2.058	2.020	2.030	2.039
	gam_dc50	---------	2.156	---------	---------	2.077	---------	---------	2.017	---------
0.5	gamma_p	2.09	2.39	2.69	1.90	2.20	2.50	1.80	2.10	2.40
	gamma_f25	2.339	2.337	2.335	2.179	2.179	2.179	2.096	2.096	2.097
	gam_dc25	---------	2.425	---------	---------	2.151	---------	---------	2.056	---------
	gamma_f50	2.264	2.264	2.263	2.124	2.126	2.127	2.054	2.056	2.059
	gam_dc50	---------	2.26	---------	---------	2.105	---------	---------	2.032	---------
1.0	gamma_p	3.04	3.34	3.64	2.14	2.44	2.74	1.95	2.25	2.55
	gamma_f25	2.973	2.971	2.969	2.356	2.356	2.356	2.182	2.182	2.182
	gam_dc25	---------	2.741	---------	---------	2.242	---------	---------	2.103	---------
	gamma_f50	2.583	2.583	2.583	2.217	2.218	2.219	2.101	2.101	2.101
	gam_dc50	---------	2.425	---------	---------	2.151	---------	---------	2.056	---------
2.0	gamma_p	4.95	5.25	5.55	2.57	2.87	3.17	2.18	2.48	2.78
	gamma_f25	4.020	4.017	4.014	2.663	2.662	2.661	2.335	2.335	2.335
	gam_dc25	---------	3.353	---------	---------	2.419	---------	---------	2.190	---------
	gamma_f50	3.115	3.115	3.115	2.382	2.382	2.382	2.187	2.187	2.187
	gam_dc50	---------	2.741	---------	---------	2.242	---------	---------	2.103	---------

Table D.1: Spectral indices from our simulation with various magnetic field configurations and γ_p values

D.4 γ vs. $b/\lambda_{\|}$

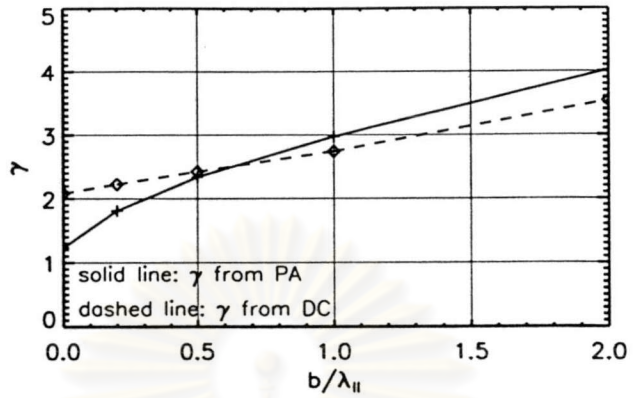

Figure D.46: Spectral index, γ, of particles with an energy corresponding with $v/U_{1n} = 25$ versus width of compression (shock $\equiv$ zero width compression region) in the cases of quasi-perpendicular shock/ compression regions, obtained from solving the pitch-angle transport equation (PA; solid line) and diffusion-convection equation (DC; dotted line).

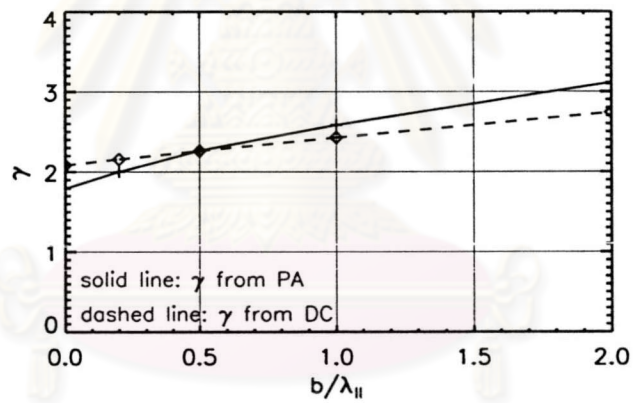

Figure D.47: Spectral index, γ, of particles with an energy corresponding with $v/U_{1n} = 50$ versus width of compression (shock $\equiv$ zero width compression region) in the cases of quasi-perpendicular shock/ compression regions, obtained from solving the pitch-angle transport equation (PA; solid line) and diffusion-convection equation (DC; dotted line).

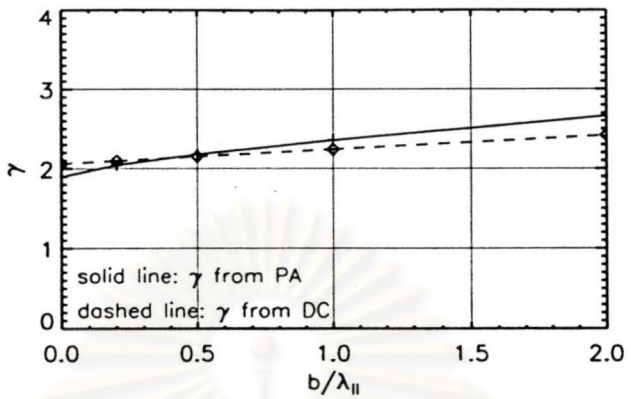

Figure D.48: Spectral index, γ, of particles with an energy corresponding with $v/U_{1n} = 25$ versus width of compression (shock $\equiv$ zero width compression region) in the cases of oblique shock/compression regions, obtained from solving the pitch-angle transport equation (PA; solid line) and diffusion-convection equation (DC; dotted line).

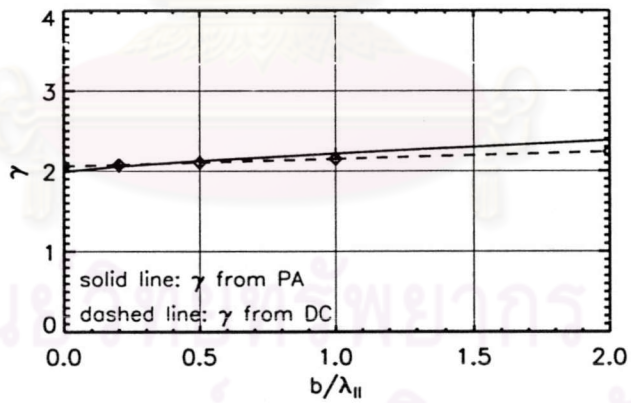

Figure D.49: Spectral index, γ, of particles with an energy corresponding with $v/U_{1n} = 50$ versus width of compression (shock $\equiv$ zero width compression region) in the cases of oblique shock/compression regions, obtained from solving the pitch-angle transport equation (PA; solid line) and diffusion-convection equation (DC; dotted line).

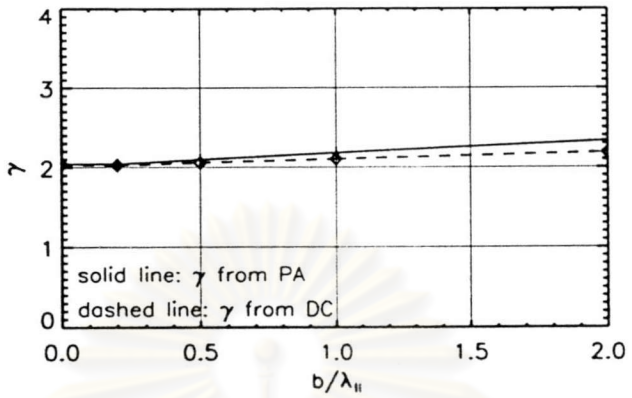

Figure D.50: Spectral index, γ, of particles with an energy corresponding with $v/U_{1n} = 25$ versus width of compression (shock $\equiv$ zero width compression region) in the cases of quasi-parallel shock/compression regions, obtained from solving the pitch-angle transport equation (PA; solid line) and diffusion-convection equation (DC; dotted line).

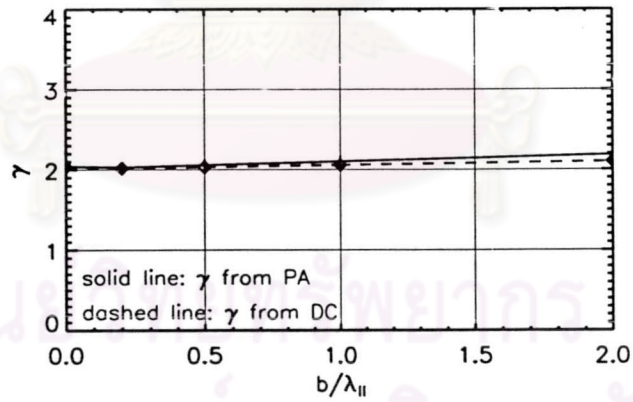

Figure D.51: Spectral index, γ, of particles with an energy corresponding with $v/U_{1n} = 50$ versus width of compression (shock $\equiv$ zero width compression region) in the cases of quasi-parallel shock/compression regions, obtained from solving the pitch-angle transport equation (PA; solid line) and diffusion-convection equation (DC; dotted line).

D.5 Decay Rate ($\ln\langle j\rangle$) vs. $z/\lambda_{\parallel}$

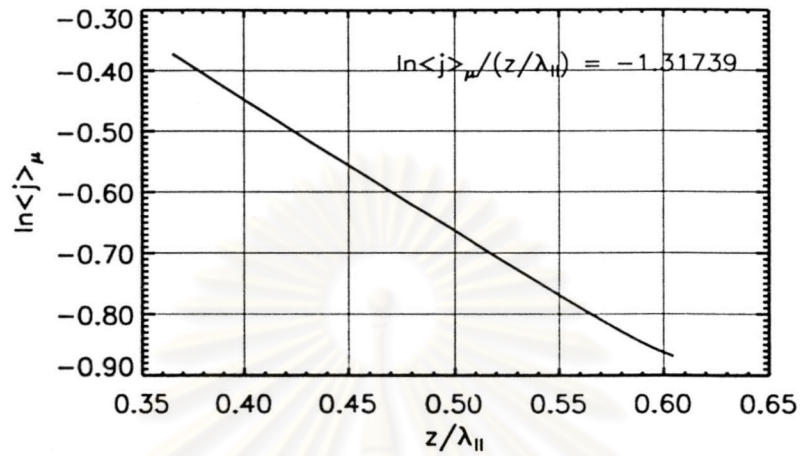

Figure D.52: $\ln\langle j\rangle_{\mu}$ vs. $z/\lambda_{\parallel}$ of a quasi-perpendicular shock, v/U_{1n}=25

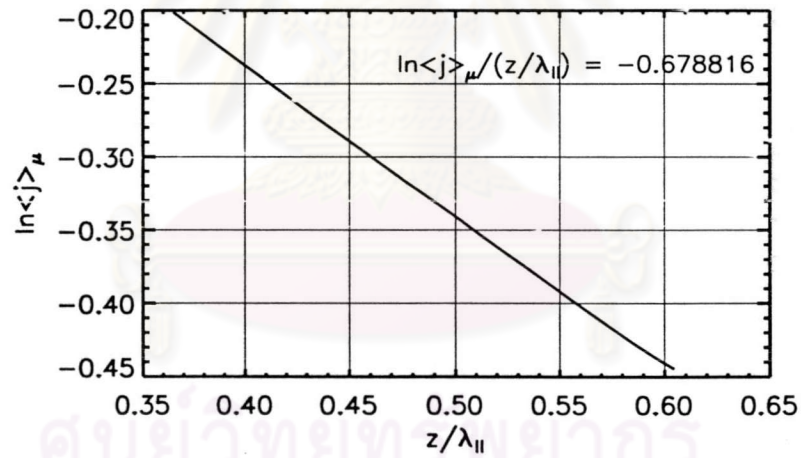

Figure D.53: $\ln\langle j\rangle_{\mu}$ vs. $z/\lambda_{\parallel}$ of a quasi-perpendicular shock, v/U_{1n}=50

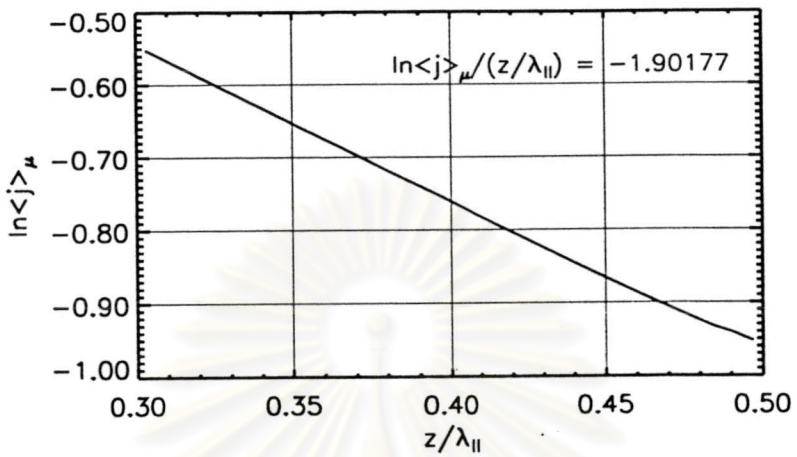

Figure D.54: $\ln\langle j\rangle_\mu$ vs. $z/\lambda_\parallel$ of a quasi-perpendicular compression region with $b/\lambda_\parallel = 0.2$, v/U_{1n}=25

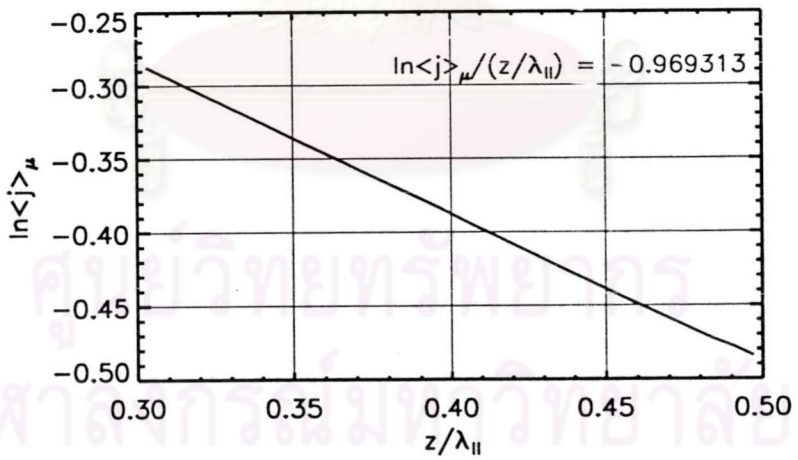

Figure D.55: $\ln\langle j\rangle_\mu$ vs. $z/\lambda_\parallel$ of a quasi-perpendicular compression region with $b/\lambda_\parallel = 0.2$, v/U_{1n}=50

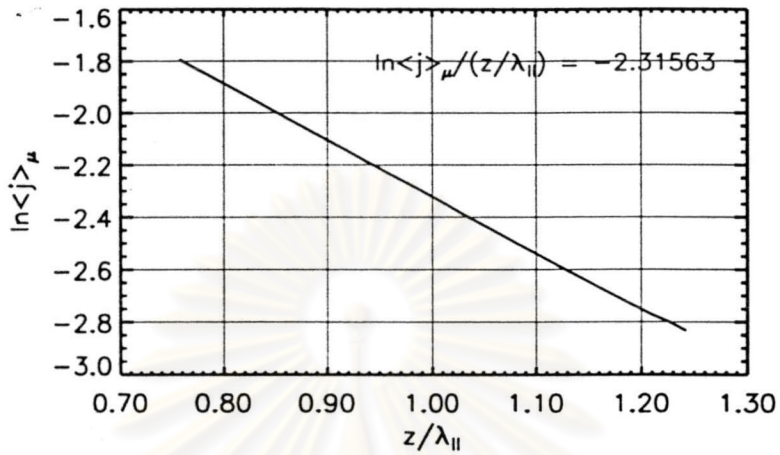

Figure D.56: $\ln\langle j\rangle_\mu$ vs. $z/\lambda_\parallel$ of a quasi-perpendicular compression region with $b/\lambda_\parallel = 0.5$, v/U_{1n}=25

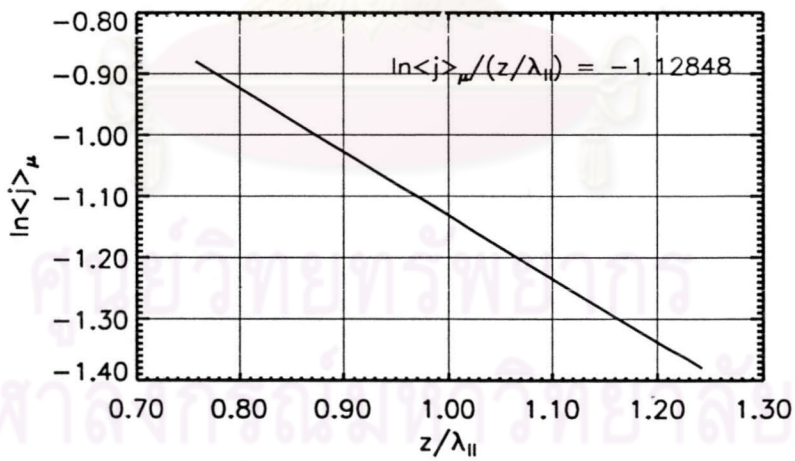

Figure D.57: $\ln\langle j\rangle_\mu$ vs. $z/\lambda_\parallel$ of a quasi-perpendicular compression region with $b/\lambda_\parallel = 0.5$, v/U_{1n}=50

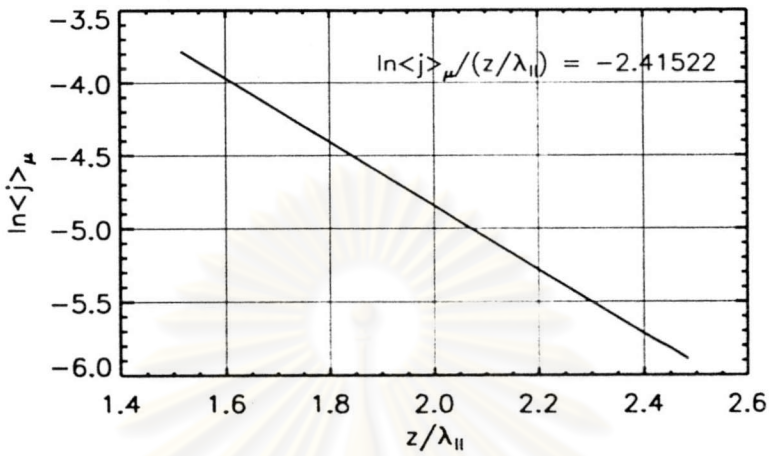

Figure D.58: $\ln\langle j\rangle_\mu$ vs. $z/\lambda_\parallel$ of a quasi-perpendicular compression region with $b/\lambda_\parallel = 1.0$, v/U_{1n}=25

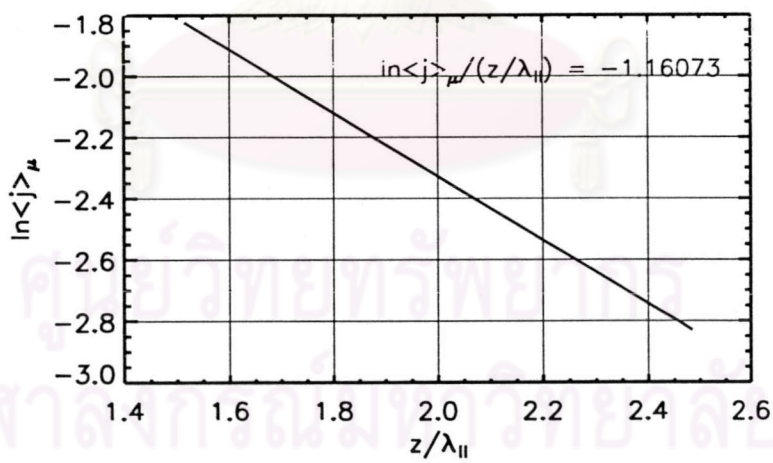

Figure D.59: $\ln\langle j\rangle_\mu$ vs. $z/\lambda_\parallel$ of a quasi-perpendicular compression region with $b/\lambda_\parallel = 1.0$, v/U_{1n}=50

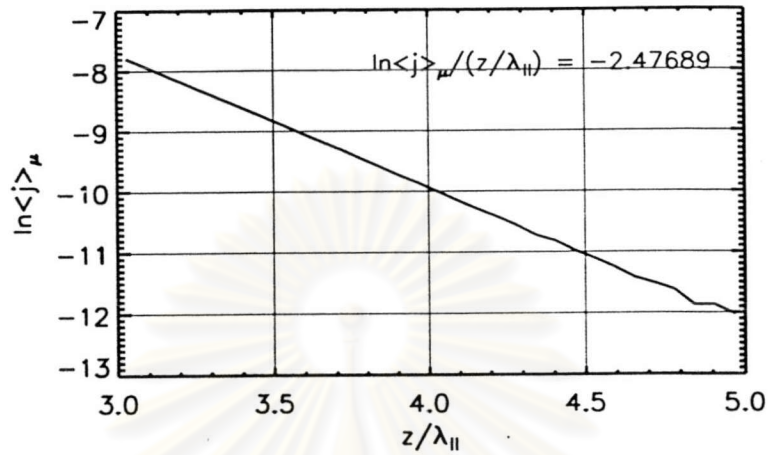

Figure D.60: $\ln\langle j\rangle_\mu$ vs. $z/\lambda_\parallel$ of a quasi-perpendicular compression region with $b/\lambda_\parallel = 2.0$, v/U_{1n}=25

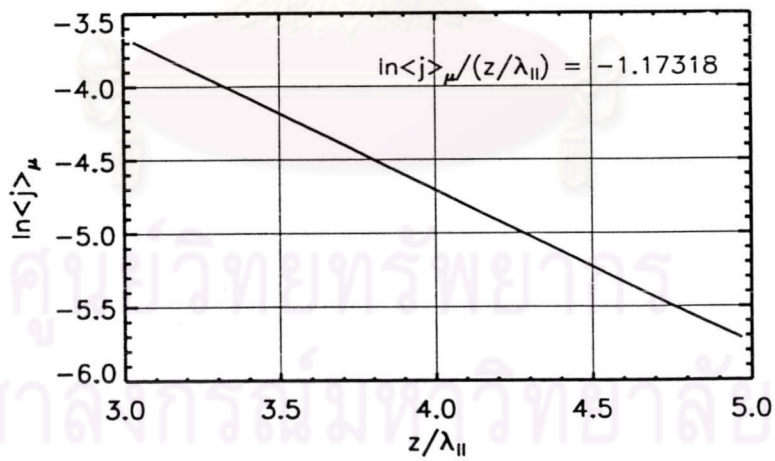

Figure D.61: $\ln\langle j\rangle_\mu$ vs. $z/\lambda_\parallel$ of a quasi-perpendicular compression region with $b/\lambda_\parallel = 2.0$, v/U_{1n}=50

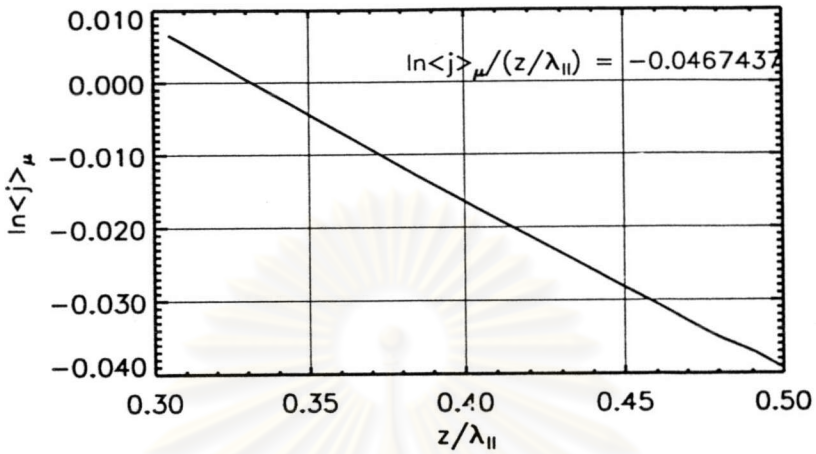

Figure D.62: $\ln\langle j\rangle_\mu$ vs. $z/\lambda_\parallel$ of an oblique shock, v/U_{1n}=25

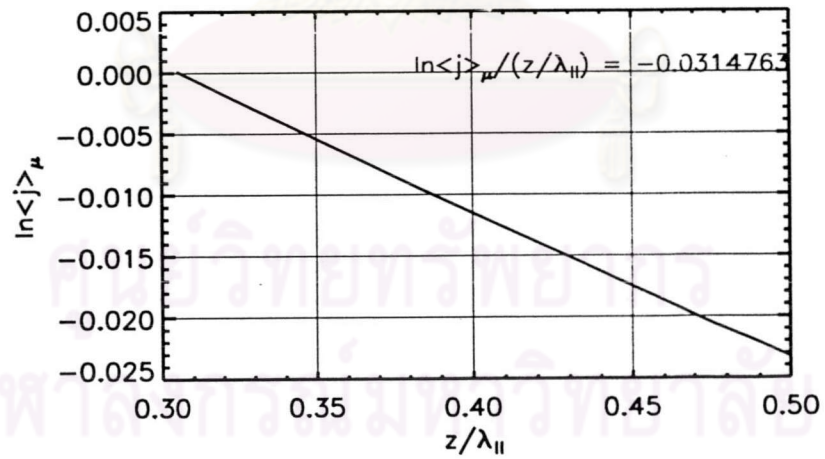

Figure D.63: $\ln\langle j\rangle_\mu$ vs. $z/\lambda_\parallel$ of an oblique shock, v/U_{1n}=50

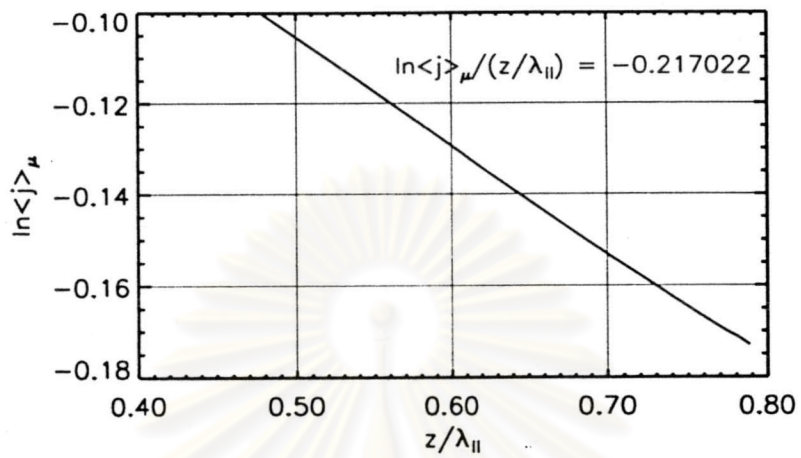

Figure D.64: $\ln\langle j\rangle_\mu$ vs. $z/\lambda_\parallel$ of an oblique compression region with $b/\lambda_\parallel = 0.2$, v/U_{1n}=25

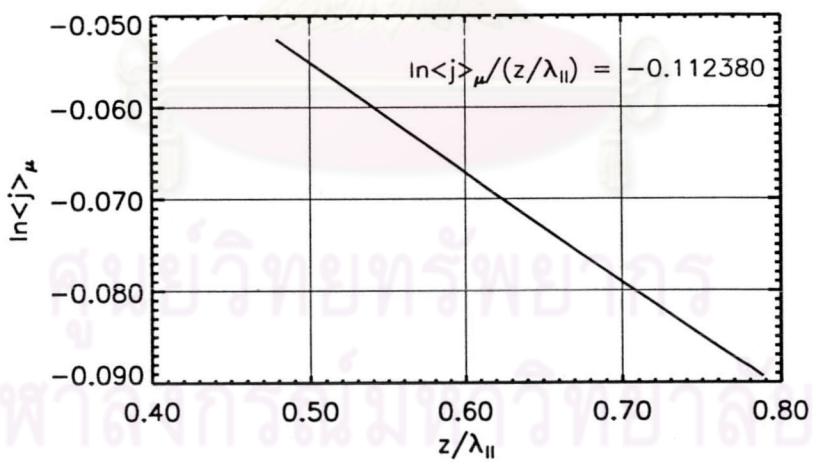

Figure D.65: $\ln\langle j\rangle_\mu$ vs. $z/\lambda_\parallel$ of an oblique compression region with $b/\lambda_\parallel = 0.2$, v/U_{1n}=50

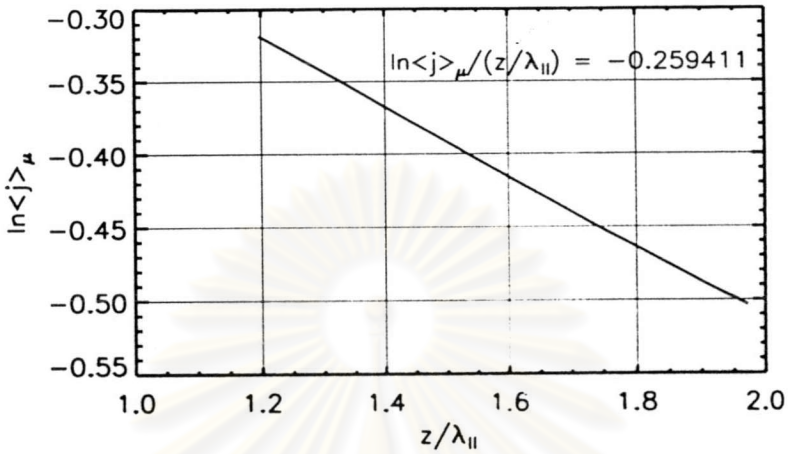

Figure D.66: $\ln\langle j\rangle_\mu$ vs. $z/\lambda_\parallel$ of an oblique compression region with $b/\lambda_\parallel = 0.5$, v/U_{1n}=25

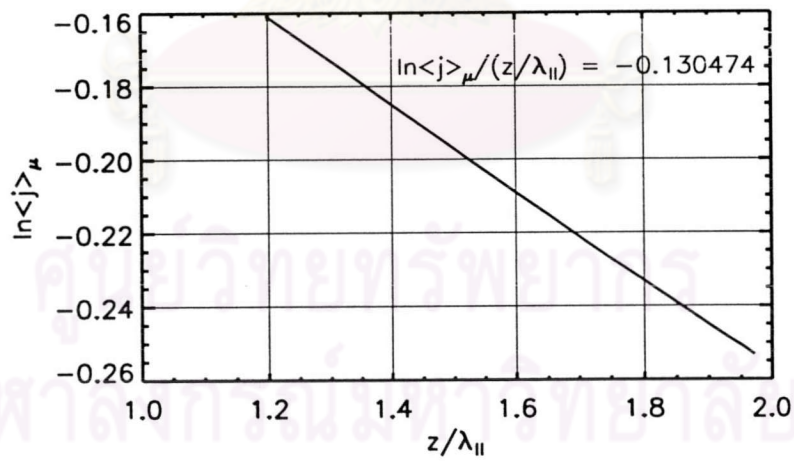

Figure D.67: $\ln\langle j\rangle_\mu$ vs. $z/\lambda_\parallel$ of an oblique compression region with $b/\lambda_\parallel = 0.5$, v/U_{1n}=50

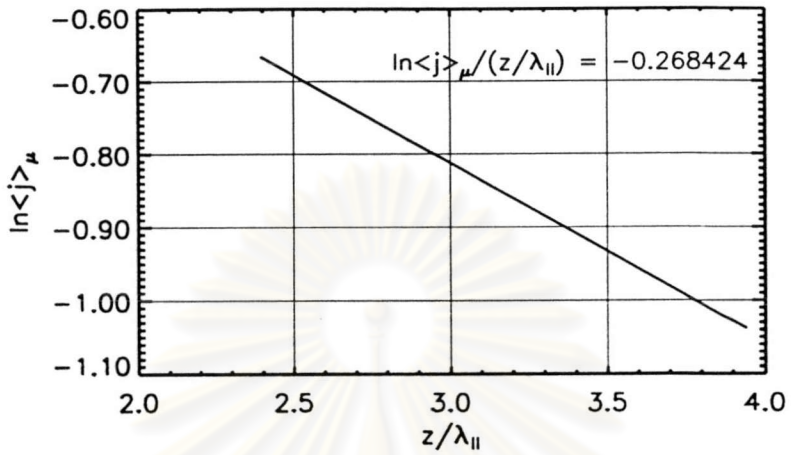

Figure D.68: $\ln\langle j\rangle_\mu$ vs. $z/\lambda_\parallel$ of an oblique compression region with $b/\lambda_\parallel = 1.0$, v/U_{1n}=25

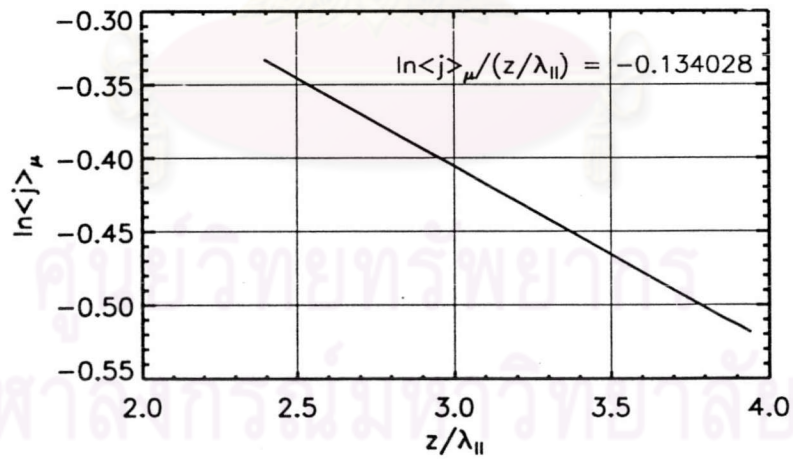

Figure D.69: $\ln\langle j\rangle_\mu$ vs. $z/\lambda_\parallel$ of an oblique compression region with $b/\lambda_\parallel = 1.0$, v/U_{1n}=50

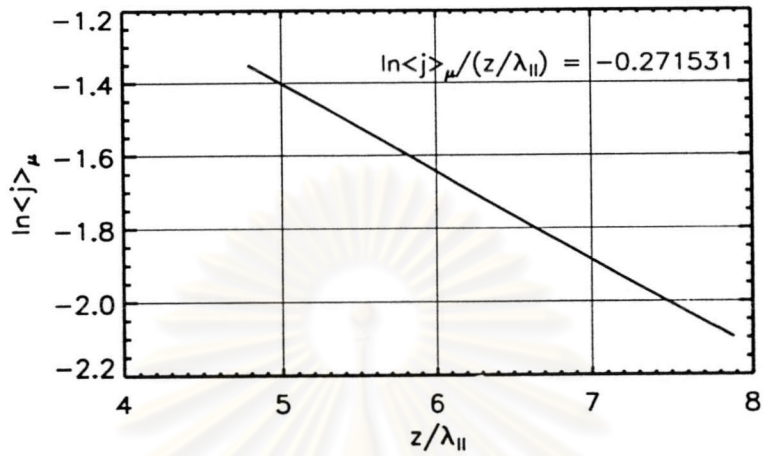

Figure D.70: $\ln\langle j\rangle_\mu$ vs. $z/\lambda_\parallel$ of an oblique compression region with $b/\lambda_\parallel = 2.0$, v/U_{1n}=25

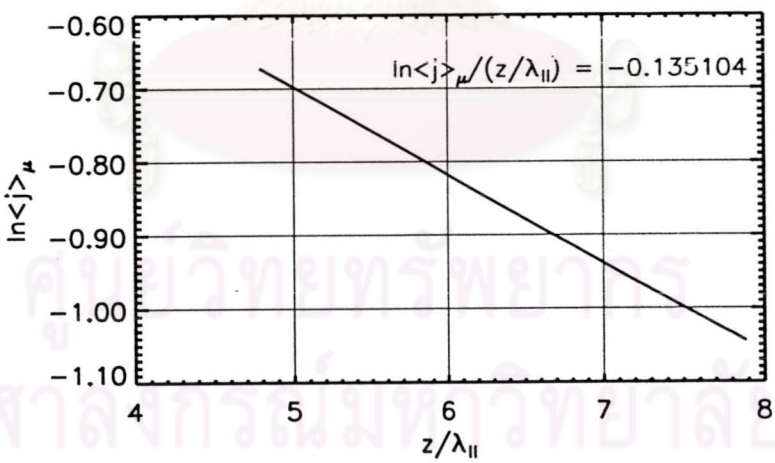

Figure D.71: $\ln\langle j\rangle_\mu$ vs. $z/\lambda_\parallel$ of an oblique compression region with $b/\lambda_\parallel = 2.0$, v/U_{1n}=50

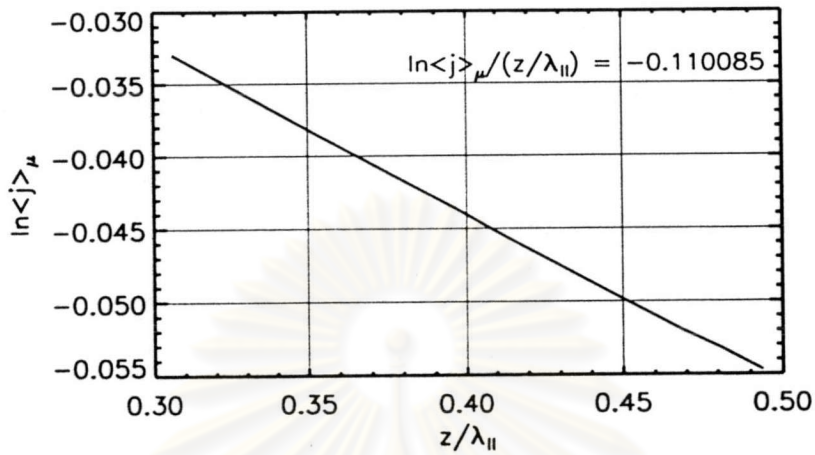

Figure D.72: $\ln\langle j\rangle_\mu$ vs. $z/\lambda_\parallel$ of a quasi-parallel shock, v/U_{1n}=25

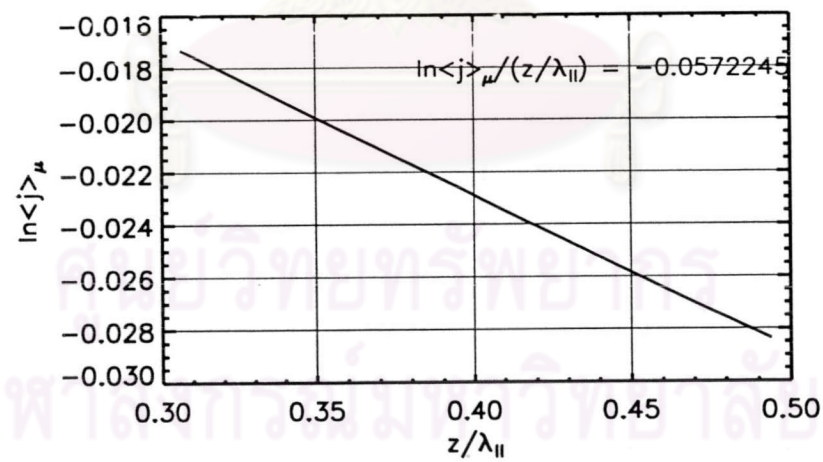

Figure D.73: $\ln\langle j\rangle_\mu$ vs. $z/\lambda_\parallel$ of a quasi-parallel shock, v/U_{1n}=50

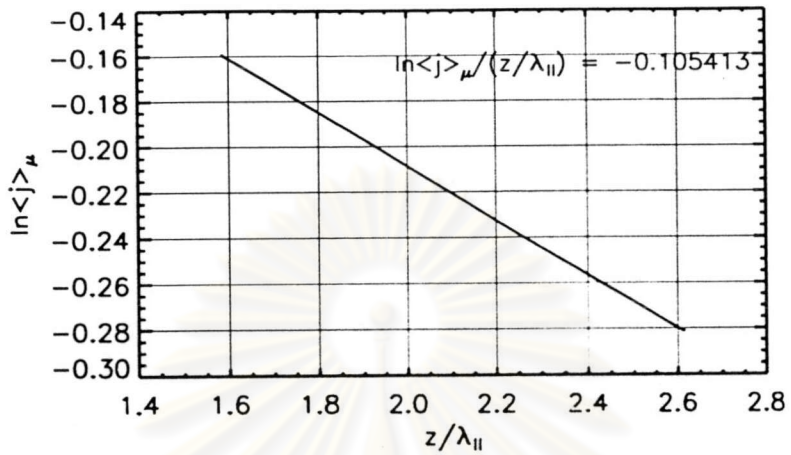

Figure D.74: $\ln\langle j\rangle_\mu$ vs. $z/\lambda_{\|}$ of a quasi-parallel compression region with $b/\lambda_{\|} = 0.2$, v/U_{1n}=25

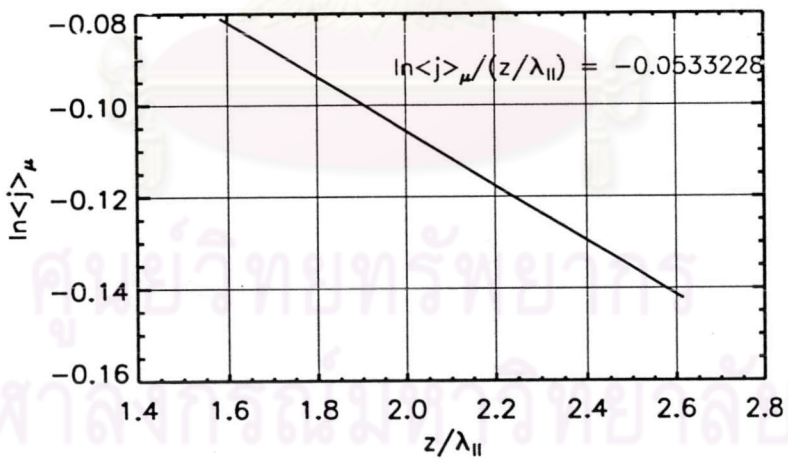

Figure D.75: $\ln\langle j\rangle_\mu$ vs. $z/\lambda_{\|}$ of a quasi-parallel compression region with $b/\lambda_{\|} = 0.2$, v/U_{1n}=50

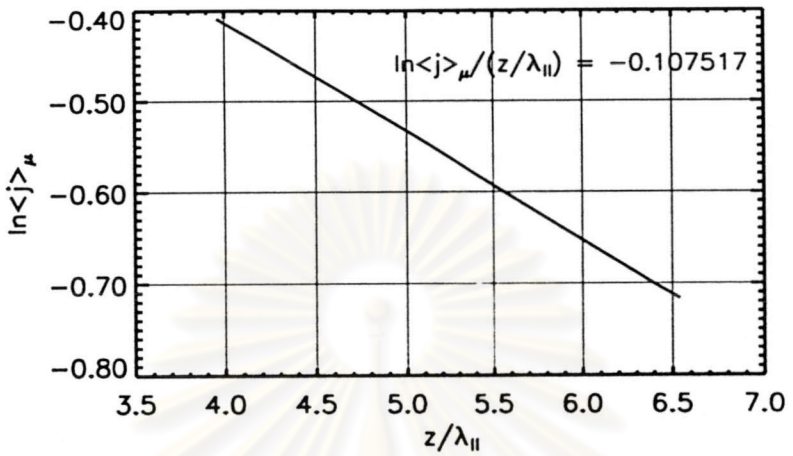

Figure D.76: $\ln\langle j\rangle_\mu$ vs. $z/\lambda_{\|}$ of a quasi-parallel compression region with $b/\lambda_{\|} = 0.5$, v/U_{1n}=25

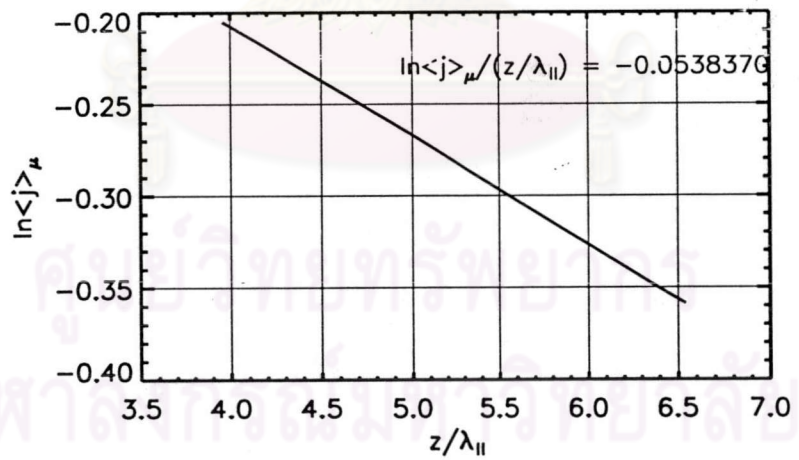

Figure D.77: $\ln\langle j\rangle_\mu$ vs. $z/\lambda_{\|}$ of a quasi-parallel compression region with $b/\lambda_{\|} = 0.5$, v/U_{1n}=50

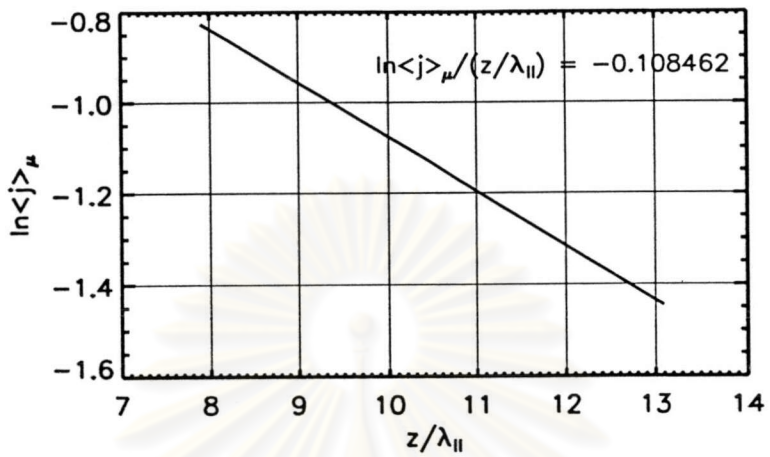

Figure D.78: $\ln\langle j\rangle_\mu$ vs. $z/\lambda_{\|}$ of a quasi-parallel compression region with $b/\lambda_{\|} = 1.0$, v/U_{1n}=25

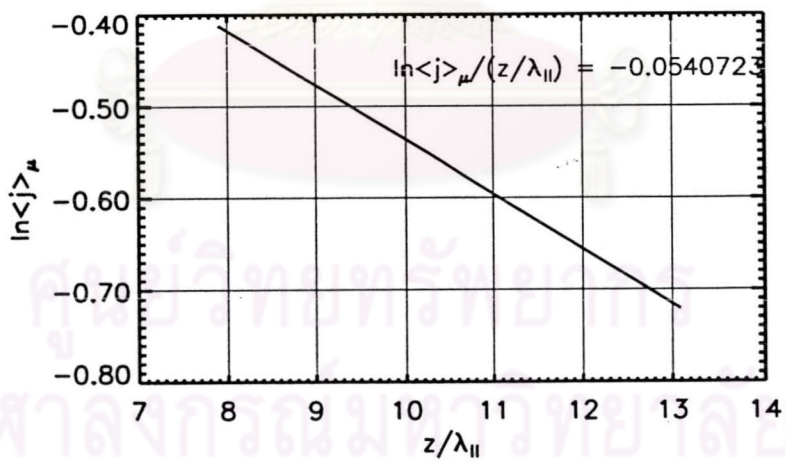

Figure D.79: $\ln\langle j\rangle_\mu$ vs. $z/\lambda_{\|}$ of a quasi-parallel compression region with $b/\lambda_{\|} = 1.0$, v/U_{1n}=50

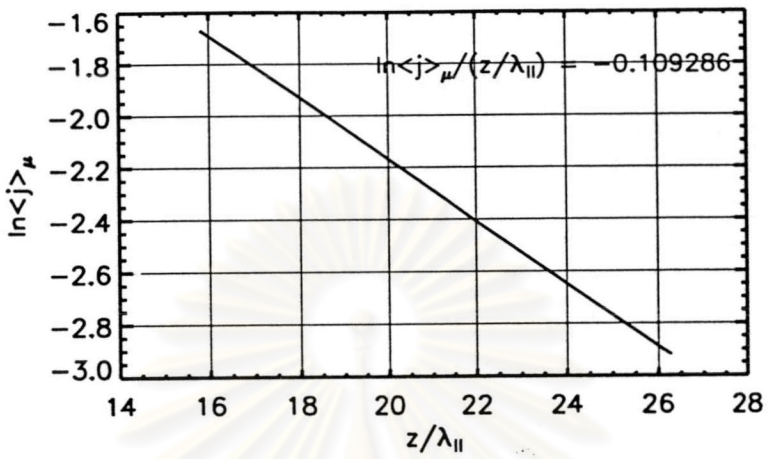

Figure D.80: $\ln\langle j\rangle_\mu$ vs. $z/\lambda_{\|}$ of a quasi-parallel compression region with $b/\lambda_{\|} = 2.0$, v/U_{1n}=25

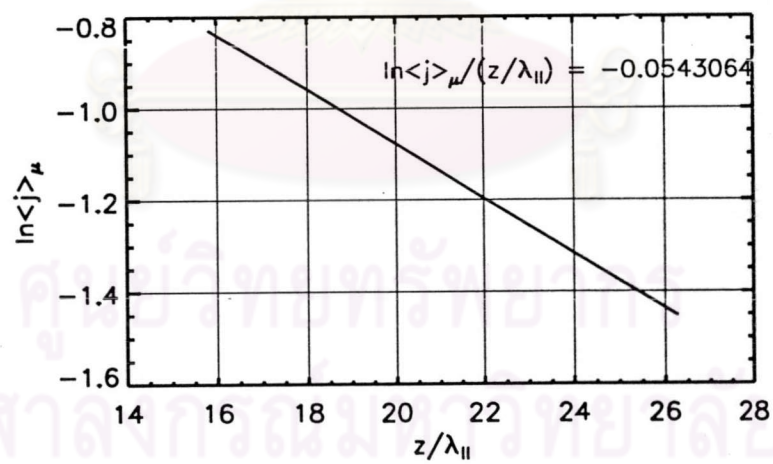

Figure D.81: $\ln\langle j\rangle_\mu$ vs. $z/\lambda_{\|}$ of a quasi-parallel compression region with $b/\lambda_{\|} = 2.0$, v/U_{1n}=50

D.6 Anisotropy (δ) vs. $z/\lambda_{\|}$

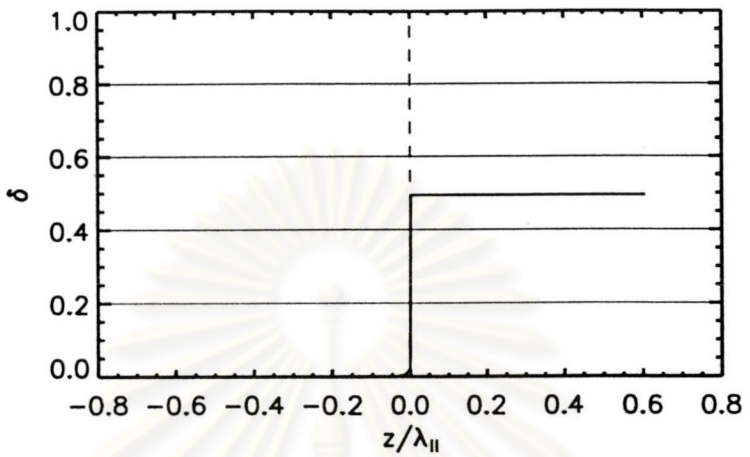

Figure D.82: δ vs. $z/\lambda_{\|}$ of a quasi-perpendicular shock, v/U_{1n}=25

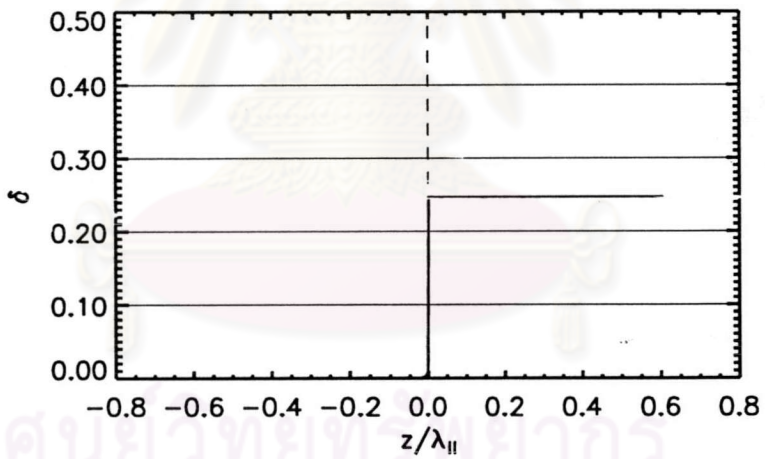

Figure D.83: δ vs. $z/\lambda_{\|}$ of a quasi-perpendicular shock, v/U_{1n}=50

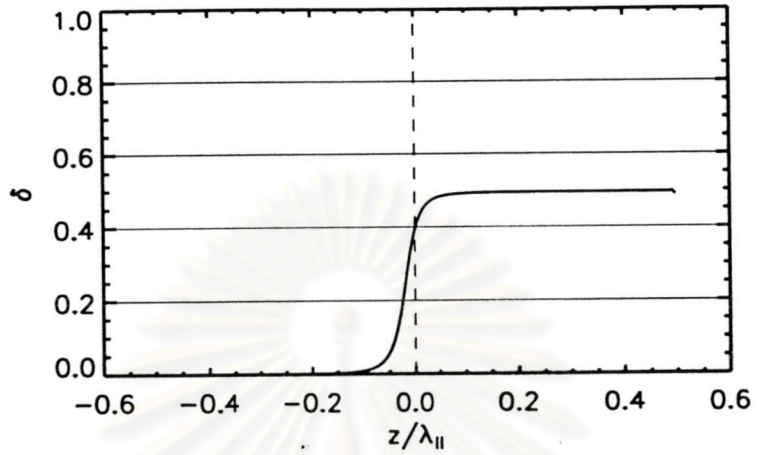

Figure D.84: δ vs. $z/\lambda_{\parallel}$ of a quasi-perpendicular compression region with $b/\lambda_{\parallel} = 0.2$, v/U_{1n}=25

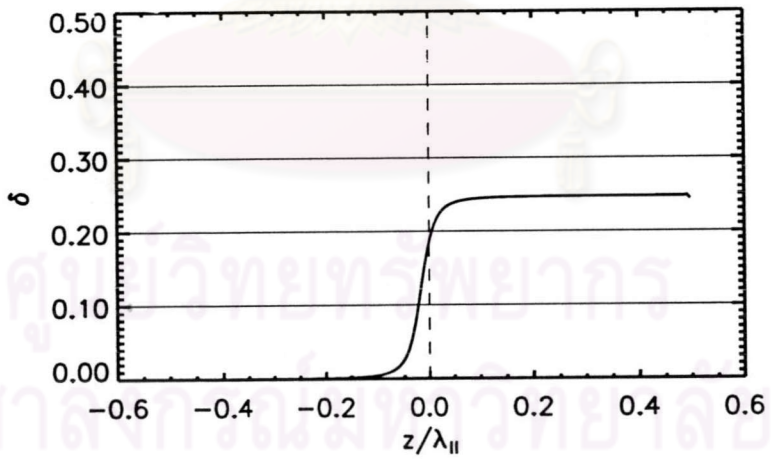

Figure D.85: δ vs. $z/\lambda_{\parallel}$ of a quasi-perpendicular compression region with $b/\lambda_{\parallel} = 0.2$, v/U_{1n}=50

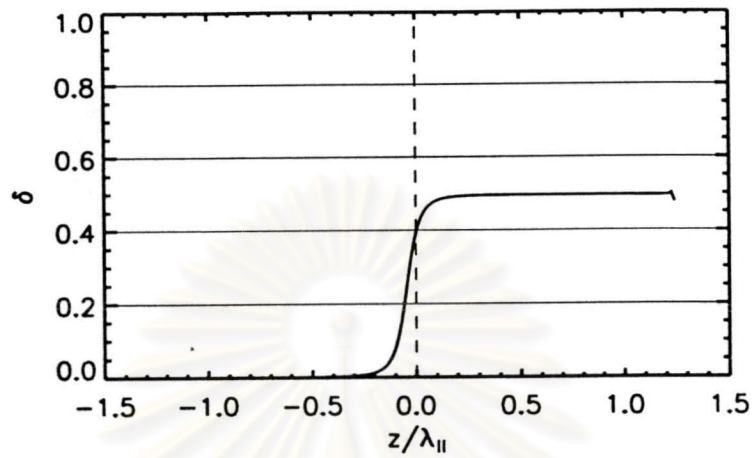

Figure D.86: δ vs. $z/\lambda_{\parallel}$ of a quasi-perpendicular compression region with $b/\lambda_{\parallel} = 0.5$, v/U_{1n}=25

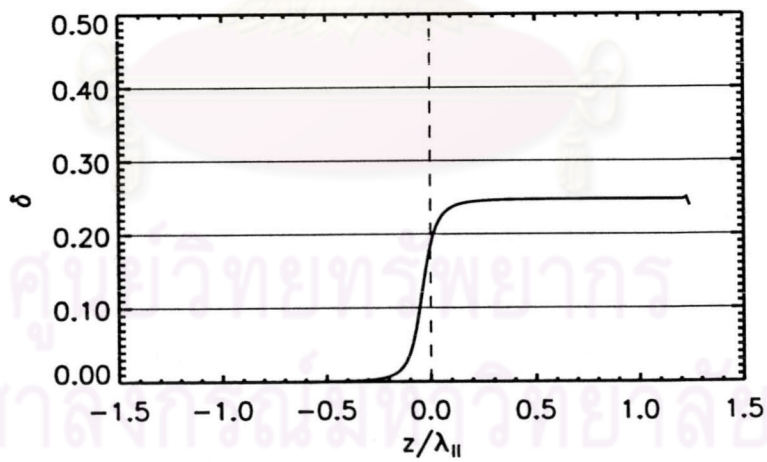

Figure D.87: δ vs. $z/\lambda_{\parallel}$ of a quasi-perpendicular compression region with $b/\lambda_{\parallel} = 0.5$, v/U_{1n}=50

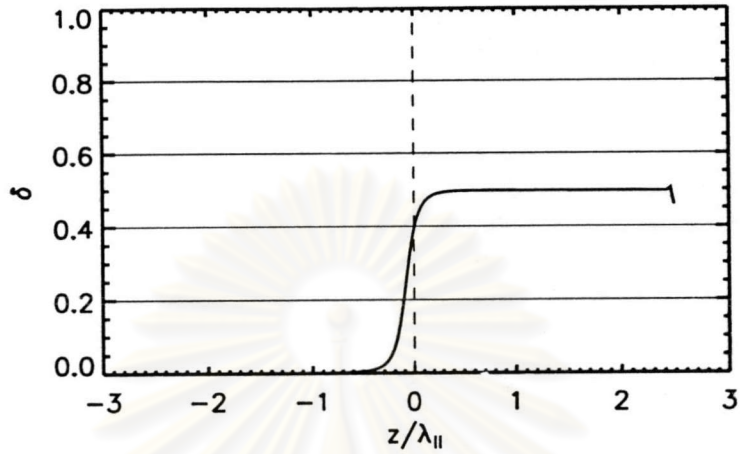

Figure D.88: δ vs. $z/\lambda_{\parallel}$ of a quasi-perpendicular compression region with $b/\lambda_{\parallel} = 1.0$, v/U_{1n}=25

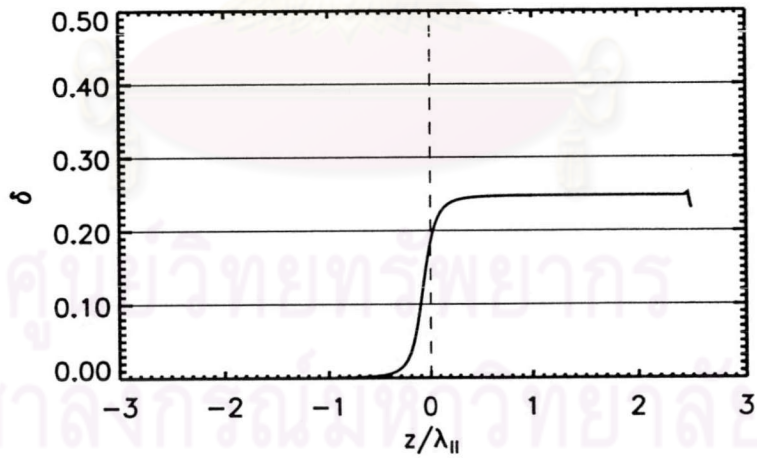

Figure D.89: δ vs. $z/\lambda_{\parallel}$ of a quasi-perpendicular compression region with $b/\lambda_{\parallel} = 1.0$, v/U_{1n}=50

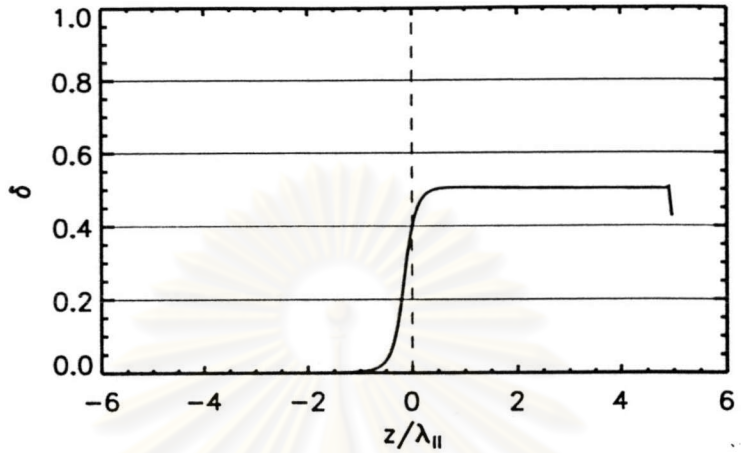

Figure D.90: δ vs. $z/\lambda_{\parallel}$ of a quasi-perpendicular compression region with $b/\lambda_{\parallel} =$ 2.0, v/U_{1n}=25

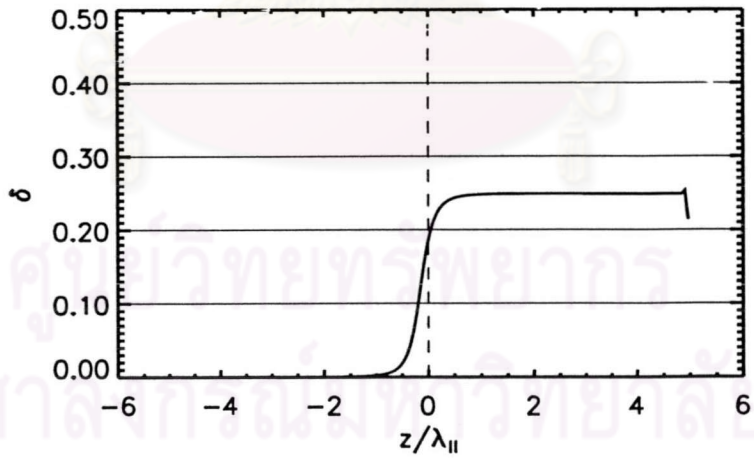

Figure D.91: δ vs. $z/\lambda_{\parallel}$ of a quasi-perpendicular compression region with $b/\lambda_{\parallel} =$ 2.0, v/U_{1n}=50

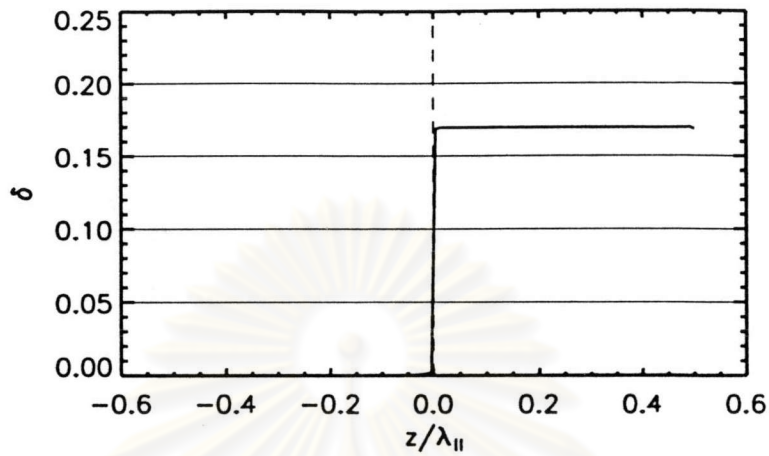

Figure D.92: δ vs. $z/\lambda_{\|}$ of an oblique shock, v/U_{1n}=25

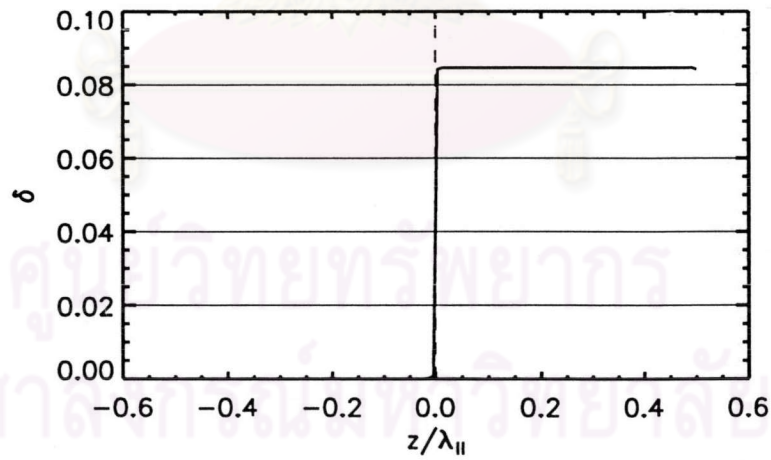

Figure D.93: δ vs. $z/\lambda_{\|}$ of an oblique shock, v/U_{1n}=50

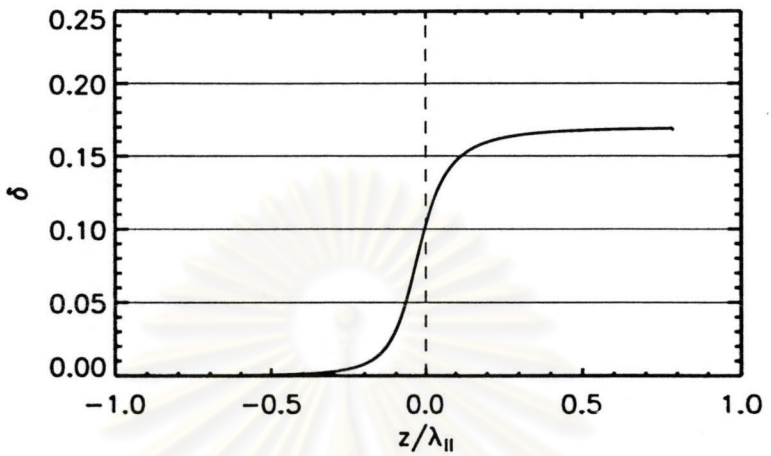

Figure D.94: δ vs. $z/\lambda_{\parallel}$ of an oblique compression region with $b/\lambda_{\parallel} = 0.2$, v/U_{1n}=25

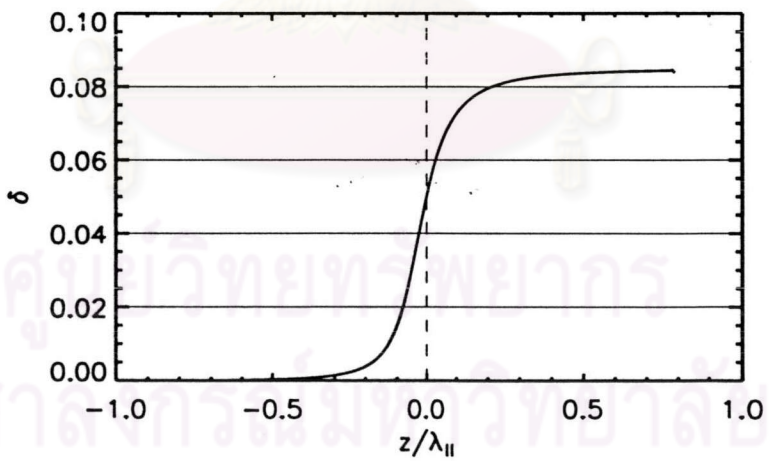

Figure D.95: δ vs. $z/\lambda_{\parallel}$ of an oblique compression region with $b/\lambda_{\parallel} = 0.2$, v/U_{1n}=50

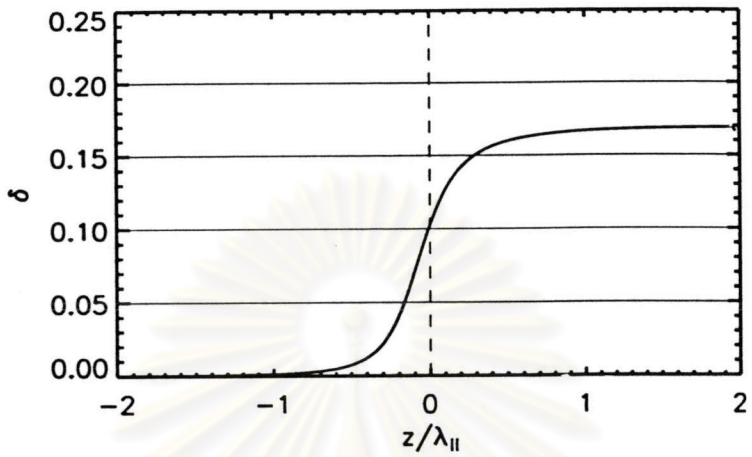

Figure D.96: δ vs. $z/\lambda_{\parallel}$ of an oblique compression region with $b/\lambda_{\parallel} = 0.5$, v/U_{1n}=25

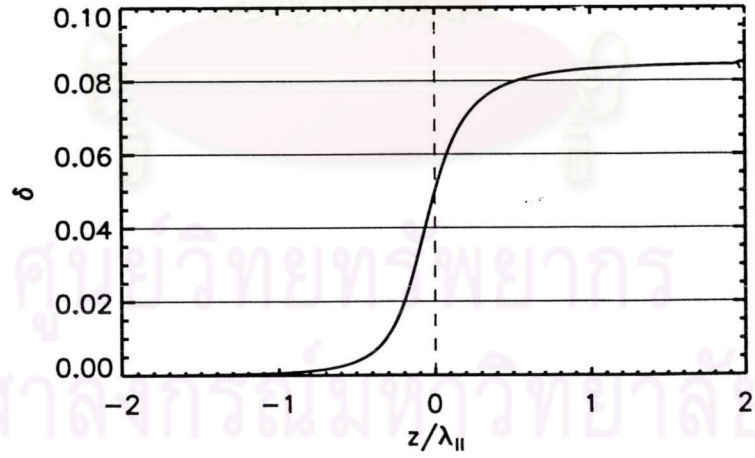

Figure D.97: δ vs. $z/\lambda_{\parallel}$ of an oblique compression region with $b/\lambda_{\parallel} = 0.5$, v/U_{1n}=50

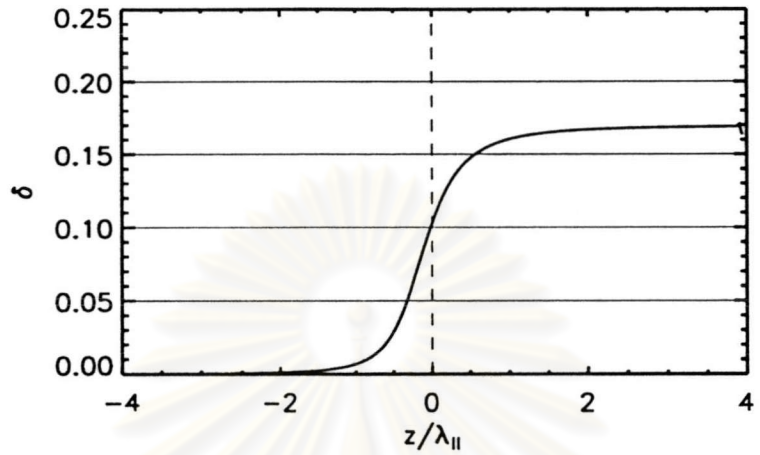

Figure D.98: δ vs. $z/\lambda_{\parallel}$ of an oblique compression region with $b/\lambda_{\parallel} = 1.0$, v/U_{1n}=25

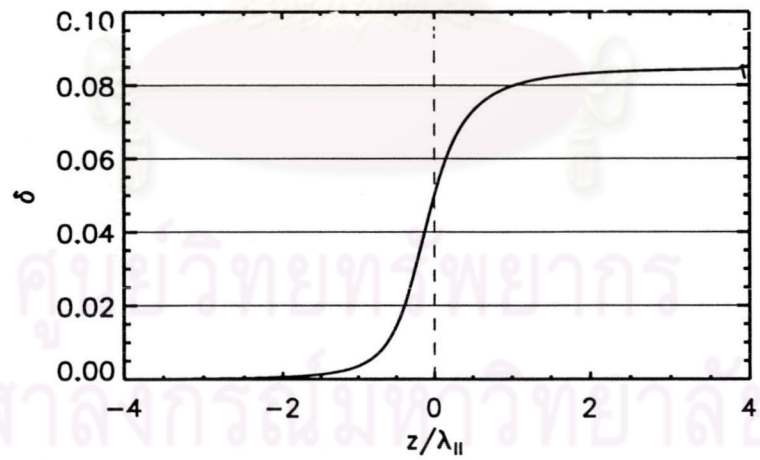

Figure D.99: δ vs. $z/\lambda_{\parallel}$ of an oblique compression region with $b/\lambda_{\parallel} = 1.0$, v/U_{1n}=50

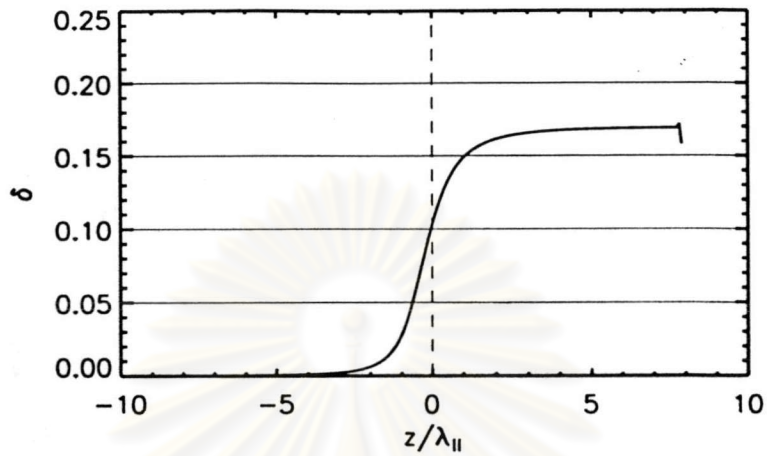

Figure D.100: δ vs. $z/\lambda_{\parallel}$ of an oblique compression region with $b/\lambda_{\parallel} = 2.0$, v/U_{1n}=25

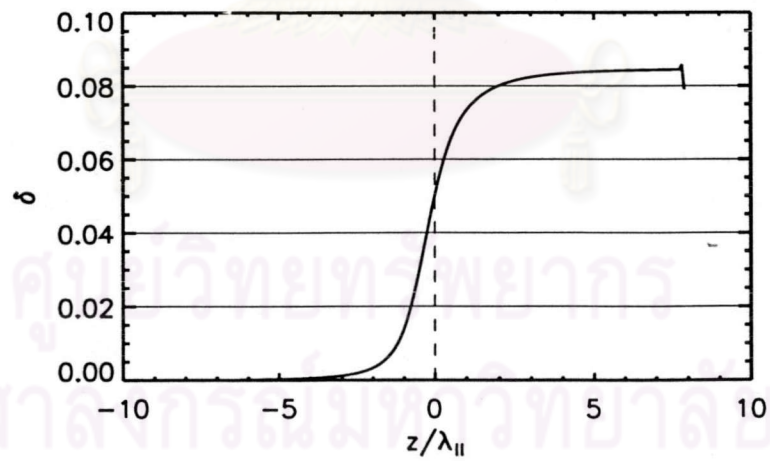

Figure D.101: δ vs. $z/\lambda_{\parallel}$ of an oblique compression region with $b/\lambda_{\parallel} = 2.0$, v/U_{1n}=50

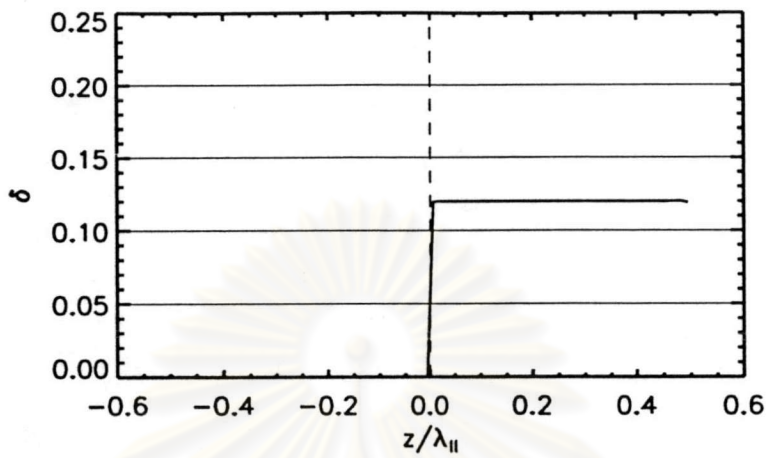

Figure D.102: δ vs. $z/\lambda_{\parallel}$ of a quasi-parallel shock, v/U_{1n}=25

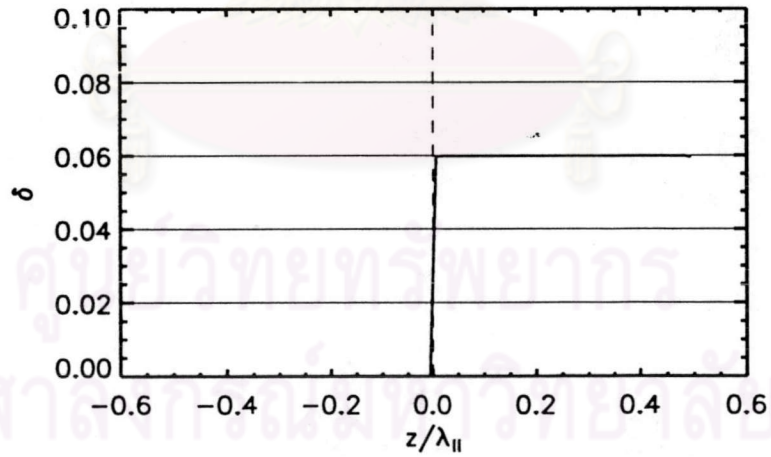

Figure D.103: δ vs. $z/\lambda_{\parallel}$ of a quasi-parallel shock, v/U_{1n}=50

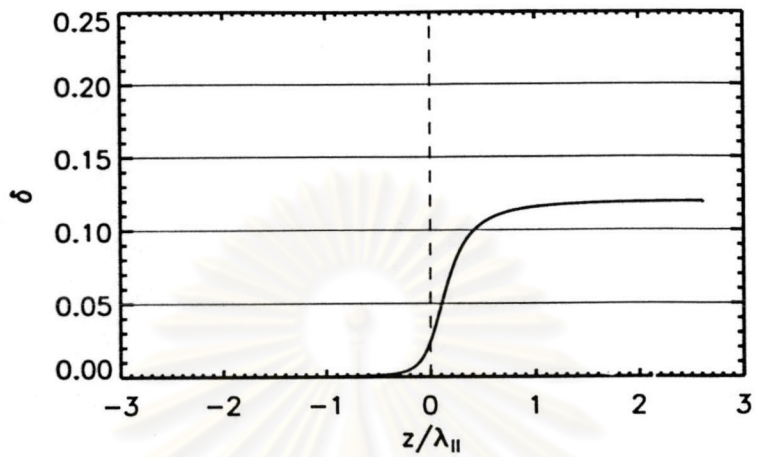

Figure D.104: δ vs. $z/\lambda_{\parallel}$ of a quasi-parallel compression region with $b/\lambda_{\parallel} = 0.2$, v/U_{1n}=25

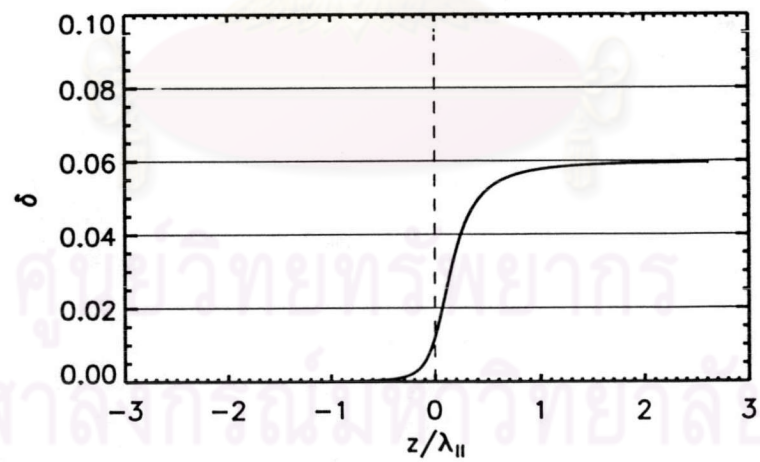

Figure D.105: δ vs. $z/\lambda_{\parallel}$ of a quasi-parallel compression region with $b/\lambda_{\parallel} = 0.2$, v/U_{1n}=50

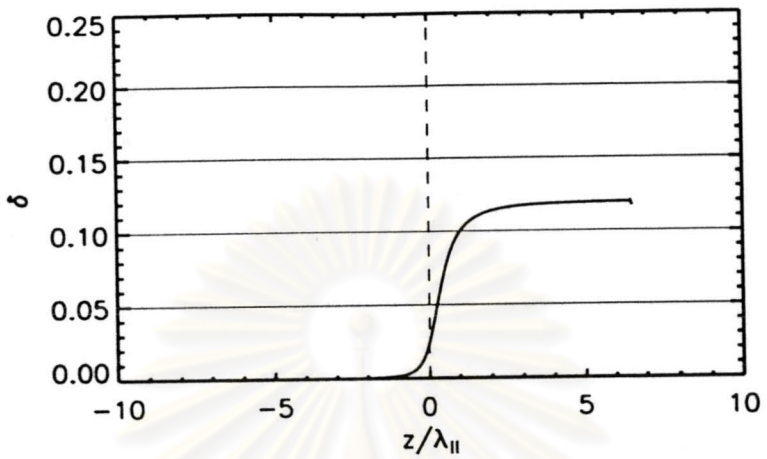

Figure D.106: δ vs. $z/\lambda_{\parallel}$ of a quasi-parallel compression region with $b/\lambda_{\parallel} = 0.5$, v/U_{1n}=25

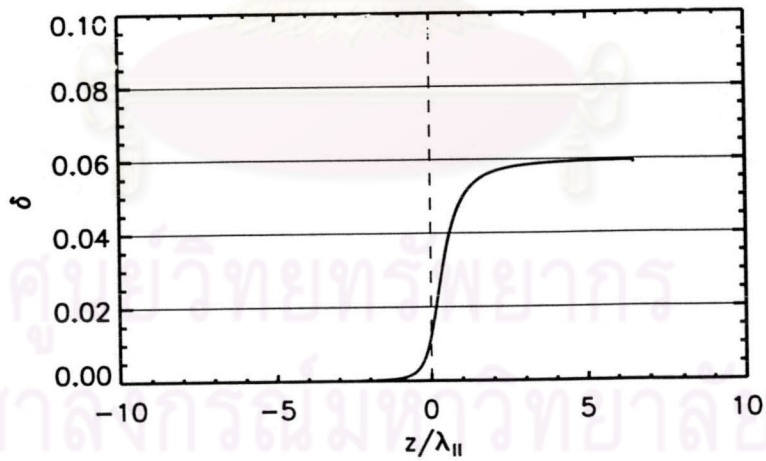

Figure D.107: δ vs. $z/\lambda_{\parallel}$ of a quasi-parallel compression region with $b/\lambda_{\parallel} = 0.5$, v/U_{1n}=50

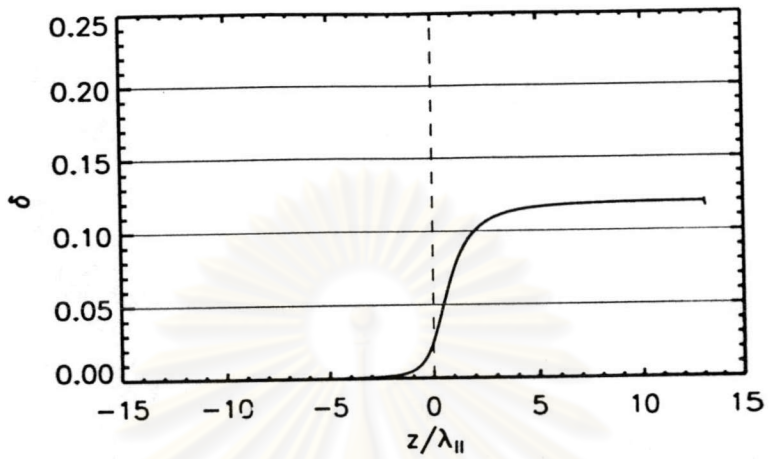

Figure D.108: δ vs. $z/\lambda_{\parallel}$ of a quasi-parallel compression region with $b/\lambda_{\parallel} = 1.0$, v/U_{1n}=25

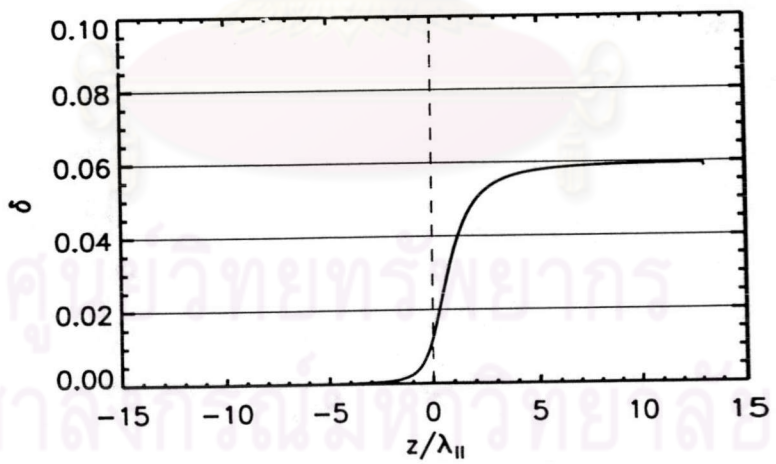

Figure D.109: δ vs. $z/\lambda_{\parallel}$ of a quasi-parallel compression region with $b/\lambda_{\parallel} = 1.0$, v/U_{1n}=50

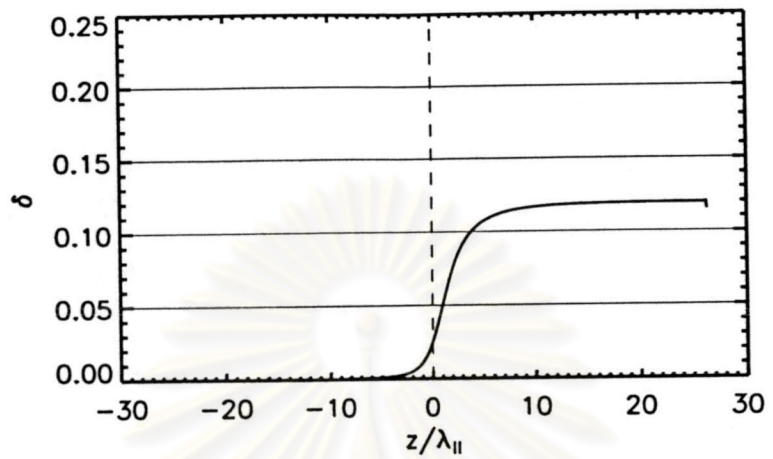

Figure D.110: δ vs. $z/\lambda_{\parallel}$ of a quasi-parallel compression region with $b/\lambda_{\parallel} = 2.0$, v/U_{1n}=25

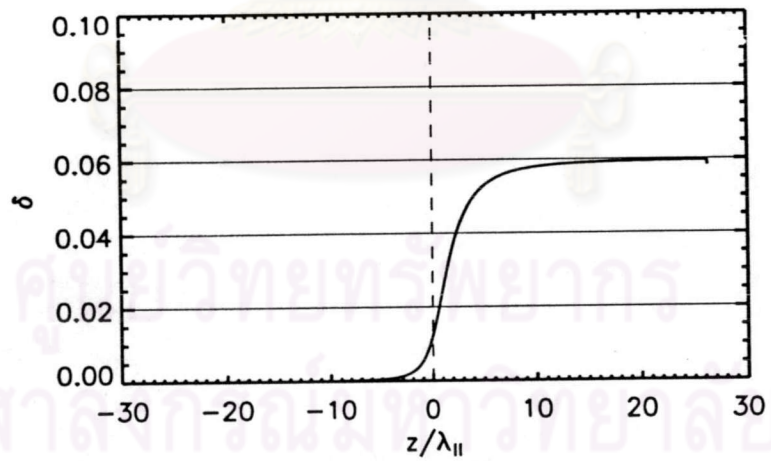

Figure D.111: δ vs. $z/\lambda_{\parallel}$ of a quasi-parallel compression region with $b/\lambda_{\parallel} = 2.0$, v/U_{1n}=50

Vitae

Name: Mr. Kittipat Malakit

Born: July 13th, 1979 in Phuket, Thailand

Farther: Mr. Khanchai Malakit, MD

Mother: Mrs. Sumitda Malakit

Education:

1999 Bachelor of Science (Physics),
King Mongkut's University of Technology Thonburi, Thailand

Conference Presentations:

2002 Malakit, K., Klappong, K.. Leerungnavarat, K., and Ruffolo, D. "Particle acceleration at regions near shocks and plasma compressions for various angles between the magnetic field and shock normal." *28th Congress on Science and Technology of Thailand (Bangkok)* (October 2002): 242.

2003 Malakit, K., Klappong, K., Leerungnavarat, K., and Ruffolo, D. "Effects of systematic pitch-angle changes on cosmic ray acceleration at shocks and compression Regions: contribution of the mirroring effect." *Proc. 7th Ann. Symp. Computational Sci. and Eng. (Bangkok)* (March 2003): 129.